University Library

MINERVA ACCESS

A gateway to Melbourne's research publications

Minerva Access is the Institutional Repository of The University of Melbourne

Author/s:
Sun, SH;Almasi, A;Yunzab, M;Zehra, S;Hicks, DG;Kameneva, T;Ibbotson, MR;Meffin, H

Title:
Analysis of extracellular spike waveforms and associated receptive fields of neurons in cat primary visual cortex

Date:
2021-04-01

Citation:
Sun, S. H., Almasi, A., Yunzab, M., Zehra, S., Hicks, D. G., Kameneva, T., Ibbotson, M. R. & Meffin, H. (2021). Analysis of extracellular spike waveforms and associated receptive fields of neurons in cat primary visual cortex. Journal of Physiology, 599 (8), pp.2211-2238. https://doi.org/10.1113/JP280844.

Persistent Link:
https://hdl.handle.net/11343/298292

Check for updates

Analysis of extracellular spike waveforms and associated receptive fields of neurons in cat primary visual cortex

Running title (70 characters max)

Analysis of cat V1 extracellular spike waveforms and associated RFs

Key words

Visual Cortex, Area 17/18, Cat, Electrophysiology, Receptive field, Extracellular spike waveform

Author names and affiliations, including postal code, email addresses

Shi H Sun[1], Ali Almasi[1], Molis Yunzab[1], Syeda Zehra[2,5], Damien G Hicks[2,3], Tatiana Kameneva[2,5], Michael R. Ibbotson[1,4], Hamish Meffin[1,5]

[1]National Vision Research Institute, Australian College of Optometry, Carlton 3053, Victoria, Australia, [2]Faculty of Science, Engineering and Technology, Swinburne University, Hawthorn 3122, Victoria, Australia, [3]Optical Sciences Centre, Swinburne University, Hawthorn 3122, Victoria, Australia, [4]Department of Optometry and Vision Sciences, University of Melbourne, Parkville 3010, Victoria, Australia, [5]Department of Biomedical Engineering, University of Melbourne, Parkville 3010, Victoria, Australia

* Authors Michael R. Ibbotson and Hamish Meffin contributed equally to this work.

Corresponding author

Michael R. Ibbotson, National Vision Research Institute, Australian College of Optometry, Carlton 3053, Victoria, Australia. E-mail: mibbotson@nvri.org.au

Table of contents category

Neuroscience

Author Manuscript

This is the author manuscript accepted for publication and has undergone full peer review but has not been through the copyediting, typesetting, pagination and proofreading process, which may lead to differences between this version and the Version of Record. Please cite this article as doi: 10.1113/JP280844.

This article is protected by copyright. All rights reserved.

Additional Information

Data availability statement

The data that support the findings of this study are available from the corresponding author upon reasonable request.

Author contributions

All experiments have been conducted in laboratories of the National Vision Research Institute, Australian College of Optometry, Victoria, Australia. H.M and M.I designed the work, conducted the experiments, interpreted the data, wrote and critically revised the manuscript. S.S conducted the experiments, analysed the data, drafted and wrote the manuscript. A.A conducted the experiments, analysed and interpreted the data and critically revised the manuscript. M.Y conducted the experiments and critically revised the manuscript. S.Z, D.H and T.K analysed the data, wrote and critically revised the manuscript. All authors approved the final version of the manuscript and agree to be accountable for all aspects of the work in ensuring that questions related to the accuracy or integrity of any part of the work are appropriately investigated and resolved. All persons designated as authors qualify for authorship, and all those who qualify for authorship are listed.

Funding

This work was supported by the Australian Research Council Centre of Excellence for Integrative Brain Function (CE140100007), the National Health and Medical Research Council (GNT1106390), and the Lions Club of Victoria.

Competing Interests

No competing interests declared.

Acknowledgements

We would like to thank Yan Wong for his valuable comments on the manuscript; and Shaun L. Cloherty, Yan Wong and Young Jun Jung for their supervision during experiments.

Author Manuscript

This article is protected by copyright. All rights reserved.

Key Points Summary

- Extracellular spikes recorded in the visual cortex (Area 17/18, V1) are commonly classified into either regular-spiking (RS) or fast-spiking (FS).
- Using multi-electrode arrays positioned in cat V1 and a broadband stimulus, we show that there is also a distinct class with positive-spiking (PS) waveforms.
- PS units were associated mainly with non-oriented receptive fields while RS and FS units had orientation-selective receptive fields.
- We suggest that PS units are recordings of axons originating from the thalamus. This conclusion was reinforced by our finding that we could record PS units after cortical silencing, but not record RS and FS units.
- The importance of our findings is that we were able to correlate spike shapes with receptive field characteristics with high precision using multi-electrode extracellular recording techniques. This allows considerable increases in the amount of information that can be extracted from future cortical experiments.

Abstract

Extracellular spike waveforms from recordings in the visual cortex have been classified into either regular-spiking (RS) or fast-spiking (FS) units. While both these types of spike waveforms are negative-dominant, we show that there are also distinct classes of spike waveforms in visual Area 17/18 (V1) of anaesthetised cats with positive-dominant waveforms, which are not regularly reported.

The spatial receptive fields (RFs) of these different spike waveform types were estimated, which objectively revealed the existence of oriented and non-oriented RFs. We found that units with positive-dominant spikes, which have been associated with recordings from axons in the literature, had mostly non-oriented RFs (84%), which are similar to the centre-surround RFs observed in the dorsal lateral geniculate nucleus (dLGN). Thus, we hypothesise that these positive-dominant waveforms may be recordings from dLGN afferents. We recorded from V1 before and after the application of muscimol (a cortical silencer) and found that the positive-dominant spikes (PS) remained while the RS and FS cells did not. We also noted that the PS units had spiking characteristics normally associated with dLGN units (i.e. higher response spike-rates, lower response latencies and higher proportion of burst spikes). Our findings show quantitatively that it is possible to correlate the receptive field properties of cortical neurons with particular spike waveforms. This has implications for how extracellular

This article is protected by copyright. All rights reserved.

Author Manuscript

recordings should be interpreted and complex experiments can now be contemplated that would have been very challenging previously, such as assessing the feedforward connectivity between brain areas in the same location of cortical tissue.

Author



Shi Hai Sun received his PhD in neuroscience at the University of Melbourne in 2019 and is currently employed as a postdoctoral researcher at the National Vision Research Institute. His PhD investigated the mechanisms underlying receptive field formation in the primary visual cortex using a newly developed set of analysis tools. Shi's interests centre on the electrophysiological properties of visual processing. In the future, he wants to pursue his interest in vision research.

This article is protected by copyright. All rights reserved.

Introduction and Background

Recordings of extracellular action potentials (spikes) have been widely used to determine the properties of individual neurons and how they communicate in networks. Typically, extracellular spikes are used to determine when a neuron has generated an action potential. In the visual system, this type of information has allowed researchers to discover the receptive field (RF) characteristics of neurons in the dorsal lateral geniculate nucleus (dLGN; Hubel and Wiesel, 1961) and primary visual cortex of cat (V1; Hubel and Wiesel, 1959, 1962). They found that cells in the dLGN had non-orientation selective, centre-surround RFs, which respond to either light ON (responding to brightness increments of light) or light OFF (responding to brightness decrements of light) in their centre. In cortex, they found elongated and orientation selective RFs with neighbouring ON and OFF regions, termed simple cells, and oriented RFs that did not have segregated ON and OFF regions, dubbed complex cells.

Intracellularly, there are four phases of the spike waveform due to the opening and closing of Na+ and K+ channels: resting membrane potential; depolarisation; repolarisation; and hyperpolarisation. Previous studies have found that temporal variations in these parameters can be used to differentiate between different neuronal classes. Broad waveforms, termed regular-spiking (RS), correspond mostly to excitatory neurons, while thin waveforms, termed fast-spiking (FS), correspond mostly to inhibitory neurons (Azouz *et al.*, 1997). This classification is also loosely supported for extracellular recordings due to the correlation between the shapes of intracellular and extracellular waveforms (Henze *et al.*, 2000).

Recently, the development of dense extracellular multi-electrode arrays (MEAs) has made it possible to sample larger areas of the brain simultaneously, with detailed identification of extracellular spike waveforms (Buzsáki, 2004). This adoption has also led to an influx of studies reporting more non-traditional waveform shapes such as spikes that are positive-dominant (Gold *et al.*, 2006, 2009; Gharat & Baker, 2017). It is possible that these new findings are due to a different sampling bias of MEAs, which do not create a confirmation bias when searching for neurons with a test stimulus, unlike that of conventional single-neuron electrophysiological recordings (Talebi & Baker, 2016; Vries *et al.*, 2020). This means that previous studies may have failed to capture a range of responses and features of neurons.

Thus, this study attempts to characterise neuronal responses in the cortex by systemically identifying extracellular spikes and associated receptive fields in V1 (defined here as Area 17

This article is protected by copyright. All rights reserved.

Author Manuscript

and 18) of anaesthetised cats. We found five distinct types of spike waveform in cat V1: RS and FS cells, as commonly identified, positive-dominant spikes, compound spikes and triphasic spikes. The RFs of the recorded units were characterised using traditional drifting sinusoidal grating stimuli and a more broadband stimulus suitable for recording from many differently tuned units simultaneously (Almasi *et al.*, 2020). The analysis, from both stimuli, revealed the existence of several types of non-oriented and oriented RFs. Spike waveform shapes and RF types were then correlated with each other. As expected, the great majority of RS and FS waveforms had orientation-selective RFs, divided into single-featured and multi-featured types, which correlate reasonably with classical simple and complex cell classifications (Touryan *et al.*, 2005). Conversely, 81-84% of positive-dominant spikes had non-oriented RFs, similar to those reported in the dLGN. We hypothesised that most positive-dominant spikes are dLGN axon afferents, likely to be axon terminals. As we cannot distinguish between axons and axon terminals, we will use the terms interchangeably. To test if we were recording from cells with their somas outside the cortex, we recorded from V1 before and after topical applications of muscimol, a potent GABA agonist that supresses local V1 activity but axons originating from other brain areas (Jin *et al.*, 2008; Vidyasagar *et al.*, 2015), and found that the positive-dominant spikes remained while the RS and FS cells did not. We also noted that the positive-dominant spikes had several spiking characteristics normally associated with dLGN units. The importance of our findings is that we show quantitatively that it is possible to correlate the receptive field properties of cortical neurons with particular spike waveforms with a high degree of certainty. This is made possible due to a range of recently developed techniques and has implications for how extracellular V1 recordings should be interpreted. It also allows complex experiments that can now be contemplated that would have been very challenging previously. For example, cortically implanted electrodes could record activity simultaneously from dLGN axon afferents as well as from the somas of V1 cortical neurons in the same cortical tissue with a single electrode penetration. This would allow very fine resolution investigation of the connectivity between brain areas.

Methods

Ethical Approval

Recordings were made from nine adult cats (Felis catus, 3M/6F, 3-6 kg). The animals were maintained in the facility at the National Vision Research Institute (NVRI), sourced from

This article is protected by copyright. All rights reserved.

Author Manuscript

Spring Valley, Victoria and Seqirus, Parkville, Victoria, and used in accordance with the National Health and Medical Research Council's Australian Code of Practice for the Care and Use of Animals for Scientific Purposes. All experimental procedures were approved by the Animal Care Ethics Committee at The University of Melbourne (ethics ID 1413312.1) and conform to the principles and regulations as described in the Editorial by Grundy (2015).

Experimental design

Animal preparation. Animals were anaesthetised with an intramuscular injection of ketamine hydrochloride (10 mg/kg), medetomidine (15 µg/kg) and methadone (0.4 mg/kg). As soon as the animal was deeply anaesthetised (absence of corneal and toe withdrawal reflexes), the animal's temperature was maintained at around 37°C with an electric blanket under feedback control, and intubated. Anaesthesia was maintained using gaseous isoflurane (1.0 – 1.5% in O_2) during surgery. During electrophysiological recordings from cortex, we switched from isoflurane to halothane (0.5 – 1.0% in a mixture of O_2 and N_2O) by means of a mechanical ventilator, because halothane has been shown to have lesser depressive effects on single-cell recordings in cat V1 (Villeneuve & Casanova, 2003). Halothane was the primary anaesthesia used for the cats. It has been shown that Halothane concentrations can be reduced but retain the same anaesthetic influence if used in conjunction with nitrous oxide (Steffey *et al.*, 1974). Therefore, we used nitrous oxide to oxygen ratios of 70:30%. The nitrous oxide was also used to offset any toxicity caused by prolonged exposure to pure oxygen (Jenkinson, 1993). The following parameters were considered in combination to determine the animal's response to anaesthesia. 1) Reflexes were absent and muscle tone is relaxed during surgical anaesthesia. We checked for a lack of pedal withdrawal reflex (i.e., toe pinch), eyelid/eyelash reflex, palpebral reflex. 2) Respiratory Sign; rate, rhythm, exhaled CO2 level, SpO2 and mucous membrane colour were continuously monitored. Deep anaesthesia was signalled by a regular rhythm and decrease in respiratory rate. 3) Cardiovascular signs and blood pressure; a slow heart rate was used as a good indication of surgical anaesthesia. An increase in rate (> 140 bpm) indicated that the depth of anaesthesia was not adequate. The concentration of gaseous anaesthesia was increased immediately in steps up to 1.5% halothane if there were persistent changes in vital signs as stated above. Data from these periods were not considered in our analysis. Our approved protocol called for the immediate I.M. injection of ketamine (5mg/kg; half of the initial anaesthetic dose) if the heart rate increased above 200 bpm (indicated by alarms), followed by detailed assessment. The blood oxygen saturation level and exhaled CO_2 level were also monitored to ensure adequate respiration. The cephalic vein

This article is protected by copyright. All rights reserved.

Author Manuscript

was cannulated for delivery of fluids and intravenous drugs. The animal was then transferred to a stereotaxic frame (with the heating blanket and additional non-heated blankets underneath all pressure points). The head was fixed using ear bars, a bite bar and a screw placed on the skull at the mid-line 30 mm anterior to inter-aural zero. A craniotomy (17mm x 12mm; P5 to A12, spanning the midline) was made to expose Areas 17 and 18 (located on the dorsal surface of the occipital cortex) in one hemisphere and the dura mater retracted. To prevent eye movements during recording, a continuous infusion was given of a neuro-muscular blocker: vecuronium bromide (0.025 to 0.05 mg/kg i.v. followed by 0.025 to 0.1 mg/kg/h). For fluid replacement, the animal received a constant intravenous infusion of Hartmann's solution (50% by volume) and 5% glucose in 0.9% NaCl solution (50% by volume) at a rate of 2.5 ml/kg/h. The animal also received daily injections of atropine (0.05 mg/kg/; s.c) to reduce salivation, dexamethasone phosphate (1.5 mg/kg/; i.m) to reduce cerebral oedema, and a broad-spectrum antibiotic (Clavulox; 0.2 ml/kg; i.m) to reduce the chances of infection. Neutral power rigid gas-permeable contact lenses were fitted onto the corneas to prevent the eyes from dehydrating. Refractive errors were assessed by reverse ophthalmoscopy and corrected using spherical lenses placed in front of the eyes. Eye drops (1% atropine sulphate; 10% phenylephrine hydrochloride) were administered daily to dilate the pupils and retract the nictitating membranes. Each experiment lasted just over three days (75 hours).

At the end of the recording, the animal was euthanised with an intravenous injection of barbiturate (sodium pentobarbital; 150 mg/kg). Animals were immediately perfused intracardially with 0.9% saline followed by 10% formol saline. The brain was extracted for later histological reconstruction of recording track locations. The histology failed to visualise complete electrode track profiles, so it was impossible to localise recording locations within specific cortical layers, but we could verify that recordings were mainly from Area 17/18 based on anatomical markers.

Visual Stimuli. Visual stimuli were presented with a ViSaGe visual stimulus generator (Cambridge Research Systems, Cambridge, UK) on a gamma-corrected LCD monitor (ASUS VG248QE, 1920 x 1080 pixels, 60 Hz, 1 ms response time) at a viewing distance of 57cm. Gamma correction was achieved by measuring the RGB luminance of the monitor (with a photodiode) and then applying an inverse transformation to the colour lookup tables (CLUTs) to each stimulus presented via the ViSaGe. The monitor was approximately centred, and stimuli were presented monocularly to the dominant eye.

This article is protected by copyright. All rights reserved.

Author Manuscript

Drifting sinusoidal gratings were presented with 100% Michelson contrast, within a circular aperture on an isoluminant grey background matched to the mean luminance of the gratings, over 30° of visual space. Orientation tuning properties were obtained by recording responses to presentations of high contrast gratings at directions of 0° to 337.5° in 22.5° increments (8 different orientations in opposite directions) and a blank condition to obtain the spontaneous activity. Each grating condition was presented in the following order: 0.5 s of the grating static; 1 s of the grating drifting (sometimes 2 seconds for cells with low temporal frequency tuning); then 0.5 s of the grating static (Fig. 1A). Each gratings condition was presented at least 5 times. After orientation tuning, we presented drifting gratings at the optimal direction at 7 different spatial frequencies (0.05, 0.1, 0.2, 0.4, 0.8, 1.6, or 3.2 cyc/deg), and then 6 different temporal frequencies (0.5, 1, 2, 4, 8, or 16 Hz) in order to obtain the optimal spatial and temporal frequencies. Drifting gratings at different orientations were then presented again with the optimal spatial and temporal frequencies. Of course, the optimal tuning properties were difficult to obtain for all cells across the MEA, so we went for the tuning properties that agreed with most recording sites.

White Gaussian noise (WGN) stimuli were used to estimate the spatial receptive fields (RFs) of visual cortical neurons. This was chosen because it is a broadband stimulus that does not require tuning to individual neurons to estimate RFs and was thus suitable for multiunit recordings. The WGN stimuli were generated through MATLAB™ with a mean value equal to the mean luminance of the display monitor (i.e. grey colour with intensity of 0.5, with 0 and 1 representing the lowest and highest luminance of the monitor, respectively). Dimensions of WGN images ranged from 45 x 45 to 90 x 90 pixels (with 15-pixel increments) depending on the size of RFs and were kept the same for the duration of each penetration. To choose the appropriate pixel dimensions, we ran a short 90 x 90 (100 images, 5 repetitions) WGN at the start, and if that was not sufficient in driving the neurons (by obtaining multi-unit post-stimulus time histograms, PSTH), we would increment down until we could sufficiently drive all (or most) of the neurons in the array. For some experiments where there were both large and small RFs, we would run two separate sets of WGN stimuli with different dimensions (e.g. 90 x 90 and 45 x 45) to sufficiently characterise all neurons in the array. WGN stimuli were presented over 30° of the visual field at 30 Hz with an OFF period (blank screen, i.e. 1/30 second WGN ON and 1/30 second WGN OFF) after each image to allow the response profile of neurons to reset, minimising any temporal correlation in the response. They were presented in blocks of 12,000 images, with the median number of

Author Manuscript

This article is protected by copyright. All rights reserved.

images in an ensemble being 192,000 (min = 96,000; max = 408,000). The standard deviation of each noise block was set to have 90% of all pixels with a value between 0 and 1. The pixel intensities were then clipped, resulting in a 10% saturation rate of the generated noise block. Noise stimuli have been used extensively in estimating RF structures (rodents: Niell and Stryker, 2008; cat: Suematsu et al., 2012). The grey-levels of WGN image pixels were drawn from an independent and identically distributed Gaussian probability distribution function. Prior to presentation of WGN on screen, the pixel intensities were converted to take on 256 different levels, ranging from 0 to 1. It is hard to predetermine how many WGN images would be needed to recover RFs. During experiments, WGN stimulus blocks were continuously presented, and an online analysis program was used to recover RFs from multi-unit activity (MUA) using spike-triggered average (STA) and spike-triggered covariance (STC) (Rust et al. 2004; Schwartz et al. 2006). Presentations of ensembles stopped once there was little change in the size, shape, and resolution of these MUA estimated RFs. Note, however, that the results presented here characterising RF used a more sophisticated off-line analysis of single unit spike trains.

Data acquisition. Neural responses were recorded using single linear 32-channel multi-electrode array (MEA) with electrodes spaced at 100 μm intervals with 177 μm^2 pad sizes from NeuroNexus. The thickness of the MEAs were 15 μm (min) and 50 μm (max), and the widths were 33 μm (min) and 240 μm (max). Electrodes were not sharpened or specially treated. After insertion, electrodes were rinsed in a stream of distilled water, soaked in a protein-dissolving detergent, and then soaked in 70% isopropyl alcohol. Following this cleaning procedure, they could be used again in another experiment. Arrays were inserted into the cortex by a piezoelectric drive (Burleigh inchworm and 6000 controller, Burleigh Instruments, Rochester, NY). Extracellular signals to the array were acquired by a CerePlex acquisition system and Central software (Blackrock Microsystems, Salt Lake City, Utah) sampled at 30 kHz for all electrode channels.

Data post-processing. The raw data was band-pass filtered using a third-order Butterworth filter, with a lower cut-off frequency at 500 Hz and an upper cut-off frequency at 14,250 Hz. Extracellular signals were automatically sorted through KiloSort (Pachitariu *et al.*, 2016), a spike-sorting program designed for dense arrays to rectify the spatio-temporal issues from extracellular recordings (i.e. spikes recorded on more than one electrode and/or neurons firing simultaneously). KiloSort uses a template-matching framework for spike detection and grouping into clusters. The outputs of KiloSort were then loaded into phy, an open source

This article is protected by copyright. All rights reserved.

Author Manuscript

visualisation interface for manual curation (Rossant *et al.*, 2016). First, clusters were "cleaned" by manually drawing a boundary in the principal component analysis (PCA) space to remove abnormal spikes outside of the boundary. For clusters that had a central dip in the autocorrelogram that did not reach zero, further manual "cleaning" was attempted by drawing a bounding in the PCA to remove batches of spikes that improved the depth of the dip in the autocorrelogram. A profound central dip, to approximately zero indicates the presence of a refractory period consistent with single unit activity. Clusters were then assigned as either "noise", which were identified with periodic peaks in the autocorrelogram and atypical waveforms (i.e. square/jagged waveforms), "good", which were identified with the presence of a refractory period (>1 ms) in the autocorrelogram with a dip to approximately zero, or "MUA", which were identified with no presence of a refractory dip to zero in the autocorrelogram. Merges were made between "good" clusters when the cluster of spikes in the PCA overlapped and their crosscorrelogram showed a >1 ms gap near zero. "Good" clusters were also merged if there was evidence of drift when the clusters had similar waveform, similar PSTH, similar autocorrelogram, and convergence in the amplitude versus time plot (i.e. one cluster stops spiking and the other starts at the same time). All "good" clusters were identified as single units (SU). The quality of each SU was quantified by calculating a signal-to-noise ratio (SNR), i.e. the ratio of the peak-to-peak amplitude of the mean waveform to twice the standard deviation of the noise (Kelly *et al.*, 2007). The mean SNR over the SU population was 2.18 ± 1.08 (SD).

Waveform Analysis and Classification

Two forms of waveform classification were used. A manual classification based on an analysis of waveform features, and an automated classification based on features extracted by wavelet analysis.

Waveform Extraction. For each single unit, up to 10,000 random spike waveforms were collected. If a single unit produced less than 10,000 spikes, then the maximum number of spikes was used (this only occurred on 10% of occasions: minimum = 1,684 spikes). For single units that were detected on more than one recording channel, the channel with the largest unsigned mean amplitude was used. Waveforms were collected in the period from 1 ms before to 2 ms after the spike time (i.e. -30 to 60 samples with 0 being the minimum or maximum peak). Collected spike waveforms were averaged and then the baseline was subtracted so that the new baseline was 0. The baseline was calculated as the mean of the first

Author Manuscript

This article is protected by copyright. All rights reserved.

and last 10 samples of the extracted waveform. For each SU, spikes with the maximum unsigned amplitude greater than six times the average unsigned amplitude of all spikes were assumed to be noise and removed. Remaining spikes were averaged to produce the waveform of that single unit. An example of an extracted waveform can be seen in Figure 1B.

Manual waveform classification. Spike waveforms were manually classified based on five features as shown in Figure 1B: amplitude, peak-trough ratio, end-slope, duration, and 1st peak-trough ratio. Amplitude is the signed difference between either the maximum peak or minimum trough and the baseline of the waveform, depending on which is larger in magnitude. Peak-trough ratio is the ratio between the unsigned amplitudes of the minimum trough and the following peak. 1st Peak-trough ratio is the ratio between the amplitudes of the minimum trough and previous peak (if it exists). Duration is the time between the minimum trough and the subsequent peak. End-slope is the gradient of the slope at a time t_s after the minimum trough. In a previous extracellular waveform study, Niell and Stryker (2008) calculated the end-slope at a defined point $t_s = 0.5$ ms after the minimum trough, for data from mice. The end-slope time for cat data has not been defined before. Here, we calculated the end-slope value at a range of post-trough times from $t_s = 0.267$ ms to 0.6 ms in 0.033 ms increments (i.e. from 8-18 samples in 1 sample increments). Note that all spike waveforms were normalised to the smallest amplitude waveform prior to end-slope calculations. To obtain the optimum end-slope time for cat spike waveforms, the end-slope and trough-peak data were normalised (using standardized z-scores) and clustered using *k*-means with two clusters (Lloyd, 1982) (see the following subsection for an intuitive description of the *k*-means clustering algorithm). Then the sum of distances of within-cluster points was calculated to obtain the distance between cluster centres. These two calculations provide information on how tight the points are within their clusters and how separated each cluster is from other clusters. The t_s value that provided the tightest within-cluster groupings and one of the largest separations between cluster was chosen.

Automatic waveform classification. Each spike waveform was decomposed into a set of wavelet coefficients by applying a 1-D discrete wavelet transform (Mallat, 1989; Akansu *et al.*, 2001). These coefficients were then used as inputs to the clustering algorithm. The reason for transforming the data prior to clustering is because, in the wavelet domain, much of the power of the spike waveform is concentrated in just a few coefficients. This reduces the effective dimensionality of the data. Wavelet decomposition is well-suited to analysis of spike waveforms because of the inherently localised nature of the features (spikes) in the

This article is protected by copyright. All rights reserved.

Author Manuscript

data. The Fourier transform, in contrast, distributes localised features over a broad range of Fourier coefficients.

The discrete wavelet transform is defined as follows (Gonzalez & Woods, 2008):

$$W_{\varphi}(j_0, k) = \frac{1}{\sqrt{N}} \sum_{n=0}^{N-1} x(n) \varphi_{j_0,k}(n) \#(1)$$

$$W_{\psi}(j, k) = \frac{1}{\sqrt{N}} \sum_{n=0}^{N-1} x(n) \psi_{j,k}(n), \text{for } j > j_0$$

where $x(n)$ represents a neural spike waveform and n indexes each of the N discrete time steps in the window of recorded activity. Here ψ is the wavelet function and φ is its associated scaling function, j and k are non-negative integers representing the scale and translation of the wavelet, respectively. j_0 is the lowest scale (resolution) level used in the decomposition. W_{φ} and W_{ψ} are the discrete wavelet transform coefficients used as inputs to our clustering algorithm, where W_{φ} are referred to as the approximation coefficients and W_{ψ} are the detail coefficients.

Wavelet decomposition involves dividing the original signals into a high and low pass component for each wavelet function $\psi_{j,k}$. The low pass component found at each level j is then treated as the input signal for the next (lower resolution) level j-1. This results in a wavelet decomposition tree (Mallat, 1989). The maximum number of decomposition levels is given by $\log_2(N)$ where N is the number of samples in the original signal. Multi-resolution wavelet decomposition was performed in MATLAB using the 1D wavelet decomposition function 'mdwtdec' and the sym4 wavelet function which resembles a Mexican-hat function.

The k-means clustering algorithm (Lloyd, 1982) was used to cluster the spike profiles into discrete groups. Each spike profile is represented as a single data point in a multi-dimensional space defined by the different wavelet coefficients. k-means clustering works by assigning each data point to the nearest cluster, where the position of each cluster is defined by the centroid of the points assigned to it. Starting from an initial guess (whose value, in our data, does not affect the final result), the algorithm iteratively refines the cluster assignments to minimise the cosine distance between the points in a cluster and the initially chosen cluster centroid. The cosine distance is a metric that measures the similarity of two vectors based on the cosine of the angle between them (Feldman & Sanger, 2007). The clustering algorithm

This article is protected by copyright. All rights reserved.

Author Manuscript

was applied in two hierarchical steps. In the first step, clustering was performed on the largest scale, i.e. lowest resolution, features of the wavelet transform, levels 5-7 (note that, in MATLAB, the convention is that higher levels correspond to larger scale features). Here we found two clusters, one corresponding to waveforms with upward positive spikes and the other corresponding to waveforms with a dominant negative peak. In the second clustering step, we performed only on the waveforms with dominant negative peaks using the higher resolution levels 2-5. The MATLAB function 'kmeans' was used.

To visualise the cluster assignments found using k-means clustering, the t-distributed stochastic neighbour embedding (t-SNE) algorithm was used. The t-SNE technique embeds the high dimensional data in a nonlinear lower-dimensional (2D) manifold (Maaten & Hinton, 2008). This provides a convenient way to visualise each waveform as a single point on a 2D plot, allowing the relative distances between different waveforms to represent the degree of similarity between them. It is important to note that the cluster assignments (found using *k*-means) are not used in the t-SNE analysis. These cluster assignments are determined prior to t-SNE dimensionality reduction and simply used to label the points on the t-SNE plot. Nevertheless, waveforms that have been assigned to the same cluster are, in general, found to be close to each other in t-SNE space.

Drifting Gratings Analysis

Drifting sinusoidal gratings were used to obtain the orientation tuning curves for each single unit. Only recordings that showed responsiveness were analysed, which is obtained from the post stimulus time histogram (PSTH) from time 0 s (start of stimulus) to 2 s (end of stimulus) in 0.1 s bins. Recordings were determined responsive if the mean response during the drifting phase (R_{drift}; between 0.6 – 1.5 s) was greater than the mean response during the static phase ($R_{static;}$ between 0.1 – 0.5 s and 1.6 – 2 s) by 1 spk/s, and the ratio between R_{drift} and R_{static} is greater than 1.3 (altogether, $R_{drift} - R_{static} > 1$ & $R_{drift} / R_{static} > 1.3$). Note the 0.1 s delay is to account for the response latency or the unit responding to the onset of the stimulus.

Receptive Field Analysis

Response latency. The response latency to WGN for each unit was determined for spike pooling in RF estimation. This was done by calculating the post stimulus time histogram (PSTH) from time 0 ms (start of stimulus presentation) to 66.67 ms (1/15 ms = the combined duration of stimulus 'ON' and 'blank' periods) in 1 ms bins. The PSTH was smoothed by applying a running average over a sliding window of length 5 ms. Latency was then

This article is protected by copyright. All rights reserved.

Author Manuscript

calculated by finding the point in time when the spike rate was >15% above the minimum ongoing spike rate. Normally a criterion significantly above baseline might be used, however, this would not be appropriate with rapid stimulus presentations.

Model estimation. Spikes were pooled into spike counts at the optimum response latency within a window of $1/30^{th}$ second corresponding to the duration of each presented WGN image. Before model estimation, all SUs were assigned a spatial region of interest that covered the RF by recovering the linear RF using STA (or STC for complex type cells) and then manually drawing a window around the spatial RF. Although the STA does not provide necessarily a complete characterisation of the RF, it is sufficient to define this region of interest and has low computational demand. For consistency, the spatial RF covered approximately a quarter of the region of interest area. As with drifting gratings, responses were deemed to be significant when the maximum response of the PSTH was greater than the minimum response of the PSTH by 1 spk/s, and the ratio between the maximum and minimum responses of the PSTH was greater than 1.3 (i.e. $R_{max} - R_{min} > 1$ & $R_{max} / R_{min} > 1.3$). Note that we use maximum and minimum here instead of the mean (as was used for drifting gratings) due to the rapid and static presentations of WGN.

RFs were then estimated using a modified version of the Nonlinear Input Model (NIM; McFarland et al., 2013) as described previously (Almasi *et al.*, 2020). The NIM has five main processing stages as shown in Figure 1C: (1) the stimulus is processed by the spatial filters; (2) passed through the corresponding input nonlinearity; (3) combined into a generator signal via summation; (4) a spiking nonlinearity is applied to produce a spike rate; and (5) the firing rate is used to randomly generate spikes according to a Poisson process. This model is described by the response r given the visual stimulus $\boldsymbol{s}$ as:

$$p(r|\boldsymbol{s}) \sim Poisson(\eta),$$

$$\eta = F\left(\sum_{i=1}^{m} f_i(\boldsymbol{k}_i \cdot \boldsymbol{s})\right), \#(2)$$

$$p(r|\boldsymbol{s};\eta) = \frac{\eta^r \exp(-\eta)}{r!}$$

where η represents the firing rate in response to $\boldsymbol{s}$ and m is the total number of filters. $\boldsymbol{k_i}$ represents the i^{th} spatial filter that processes the stimulus to produce feature-contrast (step 1), defined as their inner product $c_i = \boldsymbol{k}_i \cdot \boldsymbol{s}$. f_i is the input nonlinearity that processes the feature-contrast that can assume an essentially arbitrary form (step 2). The input signals are

This article is protected by copyright. All rights reserved.

Author Manuscript

then combined to form a generator signal ($G = \sum_{\{i=1\}}^{m} f_i(\boldsymbol{k}_i \cdot \boldsymbol{s})$ (step 3), $F(\cdot)$ is the spiking nonlinearity that converts the generator signal to the spike rate η (step 4), and then the *Poisson* process converts spike rate into spike times (step 5; last line in Equation 2).

The estimation of the parameters for the NIM (filters $\boldsymbol{k_i}$, input nonlinearity f_i, and spiking nonlinearity $F(\cdot)$) was done by maximising the log-likelihood given the neural data and stimuli. The log-likelihood (LL) of the NIM model parameters given the neural data and stimuli is:

$$LL(\boldsymbol{k}_i, f_i, F\,|r, \boldsymbol{s}) = \sum_{t=1}^{N} [r_t \log(\eta) - \eta] \quad \#(3)$$

where N are mutually independent instances of the stimuli whose responses are $\{r_1, \ldots, r_N\}$, i.e. spike counts. Note that the term $\log(r!)$ is omitted in Equation 3 because it is a constant and does not depend on the model parameters.

The number of spatial filters for each unit was determined using cross-validation by varying the number of filters and then evaluating the statistical significance of the variation with bootstrapping. Specifically, $4/5^{th}$ of the neural data were used to estimate a version of the NIM with up to five filters. The remaining $1/5^{th}$ of the data were bootstrapped (random re-sampling with replacement) to evaluate the performance of the models with different numbers of filters by calculating the log-likelihood of the filters on the remaining one-fifth of the data. This bootstrapping performance evaluation was repeated 500 times, which created a distribution for the log-likelihood for each model with different filter numbers. To determine the optimal combination of filters to use, the smallest number of filters (one filter) was used as a starting point. Then, a filter was added if the new filter significantly improved the log-likelihood (z-score > 2). Filters were incremented until there was no significant improvement in the log-likelihood. Furthermore, the combination of filters was compared against a control model, which had the filters replaced with noise (white Gaussian noise with unit variance). If the optimum model was not significantly better than the noise model, then the RF could not be estimated for that SU. We have used the approach of choosing the simplest and most compact model (smallest number of significant filters) because there are more issues with models of higher complexity; there is inevitably a compromise between complexity and accuracy (Hastie *et al.*, 2009).

Author Manuscript

This article is protected by copyright. All rights reserved.

Orientation Bias index

Orientation selectiveness of units were quantified by an orientation bias (OB) index. For data obtained from drifting sinusoidal gratings, the OB was obtained from their orientation tuning curves. For spatial RFs from model estimation, the OB was obtained by transforming the RF filter into the 2D spatial Fourier amplitude spectrum. This transforms a space representation to a frequency representation for the filter: i.e. the radial and angular coordinates of the Fourier amplitude spectrum represent, respectively, the spatial frequency and orientation of sinusoidal grating components in the Fourier decomposition of the filter. The amplitude spectrum of the transform was then sampled at the filter's preferred spatial frequency along the circular contour corresponding to 360° of direction to generate the orientation tuning curve. The orientation bias index (Leventhal *et al.*, 2003; Talebi & Baker, 2016) was then characterised, as follows:

$$OB = \left| \frac{\sum_k R_k e^{i2\theta_k}}{\sum_k R_k} \right| \#(4)$$

where R_k is the response with the spontaneous activity subtracted (the minimum R_k was subtracted instead if the minimum $R_k <$ spontaneous) for the drifting gratings data at orientation θ_k or amplitude of the Fourier spectrum for WGN data at orientation θ_k. OB values range between zero (not selective to orientation) and one (highly selective to orientation). For units with multiple filter RFs, the amplitude of the 2D Fourier spectrum for each filter was normalised and then averaged to obtain the OB. We averaged the Fourier spectra for multiple filter RFs because we believe that it best represents each neuron's overall response. For example, RFs with multiple oriented filters but with differing orientation preferences would be best represented by averaging the Fourier spectra and then obtaining the OB rather than averaging the OB for each filter.

RF size. The RF size for each SU was obtained by extracting the spatial envelopes of the filters. First, filters were rotated by their peak orientation (as described above) to obtain a vertical filter (i.e. 0° orientation). A Hilbert transform was applied to the rotated filter (along the horizontal axis of the filter) to compute the spatial envelope, and the length and width of the filter were defined as the full-width at half-maximum along the low-pass and band-pass directions of its envelope, respectively. For RFs with more than one filter, the envelopes for each filter were averaged. The Hilbert transform does not provide an accurate representation for filters with only one polarity or filters with no orientation (i.e. circular in shape). So, for

This article is protected by copyright. All rights reserved.

Author Manuscript

RFs with only one polarity, the Hilbert transform was not applied, and the spatial envelope was instead obtained with just the unsigned 2D spatial filter.

Spike train statistics

Various spike train statistics were used to compare the characteristics of the different spike waveform classes.

Driven spike rate: The driven spike rate of single units was calculated by subtracting the spike rate when the stimulus was off (spontaneous activity) from when the stimulus was on (response).

Response latency: The response latency of single units was calculated from their PSTH (as described above).

Burst Index: Two types of burst index calculations were used. The first was adapted from Wang et al. (2006) and was used to calculate the burstiness of thalamic neurons. This burst index is the ratio of burst frequency over the mean frequency for all spikes (nBurst/nAll). Spikes were defined as bursting when the inter-spike interval before the first spike was greater than 100 ms (i.e. a preceding silent period of at least 100 ms), and subsequent spikes were within an inter-spike interval of less than 4 ms. The second index was used to calculate the burstiness of cortical neurons (Snider *et al.*, 1998), which defined burst spikes as those less than 8 ms to the origin in the interspike interval distributions (0.2 ms bins and 20 ms window). We then divided the number of burst spikes with all spikes to obtain an index value between 0 and 1.

Cortical silencing

To test the hypothesis that some unit waveforms are recordings of dLGN afferents, we performed experiments to silence cortical spiking activity using the GABA agonist muscimol. For three experimental track penetrations (out of 21), 74 µL of muscimol (50 mM) was applied topically over the exposed cortical surface via a micropipette, and then another application applied topically an hour later. This was done after RFs were recovered with WGN and drifting gratings while the array was still in the cortex. The steps in the protocol were: (1) record activity in the cortex using WGN and drifting gratings stimuli; (2) apply muscimol with array still in the cortex; (3) continue to record with WGN and drifting grating presentation; (4) apply muscimol again 1 hour after the first application (top-up application);

Author Manuscript

This article is protected by copyright. All rights reserved.

(5) continue to record with WGN and drifting gratings presentation. Recording was continuous to see the effects of muscimol on the extracellular signals.

Nonlinearity characterisation

F1/F0 and F2/F1 ratios. The F1/F0 and F2/F1 ratios were calculated from drifting gratings, at the optimum orientation. The neuron's response to the drifting grating was gathered as a PSTH with a varying bin width (bin width $= \frac{1}{TF \times 6}$; TF = temporal frequency in Hz) and the spontaneous rate (response during the blank condition) subtracted. The discrete Fourier transform was then applied. The F1/F0 ratio was computed as the ratio of the first harmonic (F1; response at TF) over the 0^{th} harmonic (mean response). The F2/F1 ratio was computed as the ratio of the second harmonic (F2; response at TF $\times$ 2) over the first harmonic.

Symmetry index (SI). Characterisation of nonlinearities obtained from the NIM was based on symmetry around the zero feature-contrast of the input functions (f_i, step 2 of the NIM). The symmetry index (SI) is given by:

$$SI[f] = \frac{\|f_e\|^2 - \|f_o\|^2}{\|f_e\|^2 + \|f_e\|^2},$$

$$f_e(x) = \frac{1}{2}\big(f(x) + f(-x)\big), \#(5)$$

$$f_o(x) = \frac{1}{2}\big(f(x) - f(-x)\big)$$

Where $\|\cdot\|$ is the norm of the input function in Hilbert space, and f_e and f_o are the even and odd components of the function such that $f = f_e + f_o$. An even symmetric function $SI[f] = 1$ corresponds to $f(-x) = f(x)$, and an odd symmetric function $SI[f] = -1$ corresponds to $f(-x) = -f(x)$.

Statistical Analysis

All results are shown as the mean ± standard deviation (SD). Significance tests involving the mean were done with unpaired Student's t-tests. Hartigan's dip statistic was used to test distribution bimodality (Hartigan & Hartigan, 1985) and the significance obtained via Monte Carlo simulation, N = 10^7 (MATLAB code by Ferenc Mechler and obtained from Price, n.d.). All statistical analyses were performed using MATLAB.

Author Manuscript

This article is protected by copyright. All rights reserved.

Results

Extracellular spike waveform classes

A large number (855) of isolated single units (SUs) were recorded in V1 (Area 17/18) from 10 anaesthetised adult cats based on 21 multi-electrode array (MEA) penetrations. Spike waveforms analysed in this study refer to the mean extracellular waveform for each SU. Five classes of extracellular spike waveforms were identified as indicated in the decision tree (Figure 2A) and based on the waveform characteristics shown in Figure 1B: regular-spiking (RS, blue), fast-spiking (FS, orange), triphasic-spiking (TS, purple), compound-spiking (CS, green), and positive-spiking (PS, black) waveforms. PS waveforms had a positive peak larger than their negative trough. TS waveforms were spike waveforms with a pronounced first positive peak followed by a larger negative trough (1^{st} Peak-trough ratio >0.1) and a final positive peak < 1 ms after the first peak. CS waveforms were similar to TS waveforms but with a final positive peak > 1 ms after the first peak. RS and FS waveforms were both biphasic and had clearly dominant negative troughs, with RS waveforms having broad-shapes and FS waveforms having narrow-shapes. The RS and FS waveforms were separated from each other using clustering techniques that distinguished how rapidly the fluctuations in the waveforms occurred (see below). Individual mean spike waveforms for SUs of each extracellular spike waveform class are shown in Figure 2C, with the overall mean of each class in bold. The insets below Figure 2C show two example waveforms for each class to illustrate waveform shape variation.

While units with regular- and fast-spiking waveforms in cortex have been widely reported and studied in the literature, the remaining spike waveform types of triphasic, compound and positive-spiking waveforms have been rarely reported and have received little attention in the literature.

Regular- and Fast-spiking units

Regular-spiking units (RS, blue, n = 436, 51%) and fast-spiking units (FS, orange, n = 165, 19%) were both biphasic, i.e. a dominant negative trough (RS = 95 ± 52 μV, FS = 143 ± 77 μV) followed by either a recovery to normal levels or a smaller positive peak. It is important to note that the regular- and fast-spiking waveforms defined in this study do not equate to the ones found from *in vitro* studies. We used this nomenclature because this correlation is supported by previous studies comparing intracellular and extracellular biophysical properties (Henze *et al.*, 2000; Anastassiou *et al.*, 2015). As shown in Figure 2B, RS waveforms were

Author Manuscript

This article is protected by copyright. All rights reserved.

most abundant, comprising 51% of the overall population, followed by FS waveforms forming 21% of the overall population. The ratio of RS waveforms to FS waveforms (436/165 = 2.6) was similar to that found in other extracellular cortical studies (2.2 for cat: Chen et al., 2015; 4.1 for mice: Niell and Stryker, 2008). Broad- and narrow-spiking extracellular waveforms (RS and FS waveforms in the current study) have been associated with excitatory and inhibitory cortical cells, respectively (Barthó *et al.*, 2004). Consistent with this, the ratio of RS waveforms to FS waveforms found here is similar to the excitatory to inhibitory cell ratio identified from intracellular cortical studies (cat: Baranyi et al., 1993; monkey: Lund et al., 1979).

Following the original classification of Niell & Stryker (2008), RS and FS waveforms were separated using the end-slope (the gradient at time, t_s, after the minimum trough; as described in the Methods). The end-slope parameter was used to classify RS and FS waveforms originally in mouse visual cortex (Niell & Stryker, 2008). It was defined as the gradient of the post-spike waveform 0.5 ms after the minimum trough. However, the appropriate post-trough gradient might differ between species. For this reason, we decided to investigate a range of post-trough times to optimise the cluster separation between units, rather than simply adopting the 0.5 ms based on the rodent study.

RS and FS waveforms were separated using an end-slope of zero: i.e. spikes with an ascending slope at the chosen end-slope time (end-slope > 0) were classified as RS and spikes with a descending slope at the chosen end-slope time (end-slope < 0) were classified as FS. No units had an end-slope of zero. We used end-slope = 0 as a border between RS and FS waveforms because it provided a consistent separation for all the different post-trough times. To identify the optimum post-trough time, end-slope values at varying post-trough times, from 0.233 ms up to 0.6 ms with 0.033 ms increments, were analysed against peak-trough ratio. The post-trough time of 0.33 ms provided one of the tightest within-cluster groupings and, simultaneously, one of the largest separations between clusters (as quantified by the within cluster root mean squared error and the distance between cluster centres, respectively). Therefore, we separated RS and FS waveforms at a post-trough time of 0.33 ms. Separation of RS and FS waveforms based on end-slope at the post-trough time of 0.33 ms for the total population is shown in Figure 2D (left inset).

We also looked at the trough-peak duration (Fig. 2D; right inset) as used previously in cats (Chen *et al.*, 2015). This measure proved very robust. When plotted, RS waveforms (from

This article is protected by copyright. All rights reserved.

Author Manuscript

our analysis) were on the right of the distribution with a mean duration of 0.64 ± 0.21 ms and FS waveforms were predominantly on the left side with a mean duration of 0.27 ± 0.05 ms. Therefore, the clustering method used produced a clear binary distribution that is very similar to previous cat studies (Chen *et al.*, 2015).

Triphasic-spiking units

Triphasic-spiking units (TS, purple, n = 96, 11%) have an initial positive peak (>10% of the minimum trough), followed by a significant negative trough and then another small positive peak < 1 ms after the first. On average, the initial positive peak was 34% of the minimum trough (29 ± 22 μV / 96 ± 60 μV), which gives them their distinct triphasic shape compared to RS and FS waveforms.

Compound-spiking units

Compound-spiking units (CS, green) were also triphasic: an initial positive phase, followed by a significant negative trough, and then a slight positive peak > 1 ms after the first. The noticeable attributes of CS waveforms were their low abundance (7% of the overall population, n = 56), long waveforms with mean trough-peak duration of 1.1 ± 0.4 ms, and the smallest mean peak amplitude out of all waveform classes with mean of 53 ± 24 μV.

Positive-spiking units

Waveforms where the maximum peak was larger than the minimum trough were considered positive-spiking units (PS, black). PS waveforms were moderately abundant with 12% of the overall population (n = 102) and mean amplitude of 92 ± 40 μV. Evident in the traces in Figure 2C and the inset below, PS waveforms vary considerably in shape. Sixty-one percent of PS waveforms were biphasic (n = 62; example shown in the left inset), which had a maximum positive peak followed by a slight negative trough. Thirty-six percent of PS waveforms were triphasic (n = 37) in which there were two significant positive peaks with a small trough in between (i.e. M shaped, example shown in the right inset). The remaining (n = 3) had >3 phases in their waveform.

Classification comparison

To determine the reliability of our manual classification method described above, we also automated the classification of our SUs using wavelet decomposition and the *k*-means clustering algorithm to assign each spike waveform to one of four clusters (see Methods). Only four groups were used in the automated classification compared to the five in the manual classification because of the low population of TS and CS waveforms (11% and 7%,

This article is protected by copyright. All rights reserved.

Author Manuscript

respectively). CS waveforms are also a subcategory of TS waveforms (see Fig. 2A), which the k-means struggled to separate due to the low variability in the two clusters. We then examined how these automated cluster assignments compared with those determined using the manual classification method.

The automated method classified the 855 units into four categories: #1; #2; #3; and #4. Individual mean spike waveforms for each SU for each category are shown in Figure 3A, with the overall mean of each class shown in bold. The waveform shapes of classes #1, #2, #3 and #4 closely correspond to RS, FS, TS/CS and PS waveforms, respectively (i.e. waveforms in #2 have a short trough-peak duration, similar to FS waveforms, #4 are mostly positive, similar to PS waveforms, etc). This close correlation can also be seen in the population statistics in Figure 3B, which show the proportion of RS, FS, TS, CS and PS waveforms for each automated class. If we were to assume classes #1, #2, #3 and #4 correspond to RS, FS, TS/CS and PS waveforms, respectively, then 71% of SUs (606/855) were classified into the same class using both methods, which indicates that the manual method generalises fairly well with the automated method. This similarity between classification methods is also evident if we use a technique for visualisation of high-dimensional datasets in two dimensions (Fig. 3C; t-distributed stochastic neighbour embedding plots; t-SNE; Maaten and Hinton, 2008).

From here on, we will use the manual classification method for three reasons. (1) The manual classification method uses a set of features that are associated with the spike shape based on previous work in the literature (Niell & Stryker, 2008; Gold *et al.*, 2009), and is easy to replicate by others. (2) The automated classifier produces more outliers, as is evident in the individual traces in Figure 3A and the separation of some data points from their clusters in the t-SNE plots (Fig. 3C). Unlike the manual system, it is not possible to set fixed classification parameters so that others can replicate this automated analysis precisely. (3) We want a clear category for triphasic waveforms, which the automated method could not robustly classify into a separate group (i.e. the mean waveform from #3 is biphasic). Importantly, both methods clearly separated the cluster of PS waveforms from all other waveforms.

Characterisation of receptive fields

For the 855 SUs outlined in the previous section, all were visually stimulated with drifting sinusoidal gratings and white Gaussian noise (WGN) to characterise their receptive fields.

This article is protected by copyright. All rights reserved.

Author Manuscript

According to our criteria (see Methods), 52% of units (n = 442) responded to WGN, 74% (n = 633) responded to drifting gratings, and 87% responded to either WGN or drifting gratings. This leaves 13% of units that could not be visually stimulated, which is lower than that found in mice (Vries *et al.*, 2020).

RFs recovered with WGN

Out of the 442 SUs that responded to WGN, 325 had their RF successfully recovered using the nonlinear input model (NIM) (see Methods). We noticed that RFs fell into two categories: the first contains units with one or more classically oriented RF filters (example in Fig. 4A left); the second contains units with one or more non-oriented RF filters that were approximately circular (example in Fig. 4B right). Units with more than one RF filter mean that they have multiple preferred spatial features. Non-oriented receptive fields have been reported before in the visual cortex of cat (Talebi & Baker, 2016; Gharat & Baker, 2017) and monkey (Ringach, 2002). In some units, the non-oriented filters had a weak surround of opposite polarity. The degree of orientation selectivity was quantified by an orientation bias index (OB), which was obtained by transforming the RF filter into the two-dimensional (2D) Fourier domain (middle row of Fig. 4A). This allows the amplitude spectrum of the filter to sinusoidal gratings of a given spatial frequency and orientation to be represented by the radial and angular coordinates of the Fourier spectrum, respectively. The orientation tuning curve (bottom row of Fig. 4A) was obtained by sampling the amplitude of the transform along the circular contour corresponding to all 360° of orientation at the filter's preferred spatial frequency (black dashed circle). The OB could then be obtained from the orientation tuning curve (Eq. 4).

Figure 4B plots a histogram of the number of units as a function of their OB, showing a bimodal distribution. The distribution is significantly different from unimodality (Hartigan's dip test, $p = 10^{-5}$). Units were divided into oriented RFs with OB > 0.2 (n = 231, 71%) and non-oriented RFs with OB < 0.2 (n = 94, 29%). This division has been used previously for cat Area 18 data (Gharat & Baker, 2017) as well as LGN neurons, which typically have an OB < 0.2 (Rosenberg *et al.*, 2010). Several example RFs are shown in Figure 4C, starting with circular and unoriented RFs of OB values close to 0 and then more oriented and elongated RF filters as the OB increases. Note that Talebi and Baker (2016) used a division between RF classes of OB = 0.1, while we used 0.2. Like us, they obtained their OB from the spatial filters rather than from the neuron's response to drifting gratings. Later, they did a separate study using gratings (Gharat & Baker, 2017) with a 0.2 separation. We chose a

This article is protected by copyright. All rights reserved.

Author Manuscript

division at 0.2 because our data shows a clear separation at OB = 0.2 in the histogram of Figure 4B and RFs with OB values between 0.1 and 0.2 had circular, unoriented shapes (Fig. 4C).

RF size was also measured by extracting the spatial envelopes of the filters (see Methods). The mean RF length for oriented RFs was 2.62° ± 1.86°, which was significantly larger (student's t-test, $p = 10^{-9}$) than for non-oriented RFs: 1.40° ± 0.65°. The mean aspect ratios (length/width) of oriented and non-oriented RFs were 0.93 ± 0.34 and 0.96 ± 0.37, respectively.

We further divided oriented units (OB > 0.2) into single-feature RFs (SRF) for units with only one filter, and multi-filter RFs (MRF) for units with more than one filter. This puts our population of RFs into three groups in total: SRFs that have a single oriented filter (n = 152/325 = 47%); MRFs that have multiple filters with an overall oriented RF (n = 79/325 = 24%); and single or multiple filters with an overall non-oriented RF (blob RFs, n = 94/325 = 29%). Single and multi-filter RFs have been correlated with simple and complex cells, respectively, in cat V1, although the association is not perfect (Touryan *et al.*, 2005; Almasi *et al.*, 2020).

Relationship of RFs recovered with WGN to waveform classes

Having established our classes of spike waveforms and our classes of RFs from WGN, we next wanted to see if the different spike waveform groups were associated with specific RF types (i.e. correlating spike shapes and RF properties). Figure 4D is a bar graph showing the number of RF types for each spike waveform type (n RS = 120, FS = 91, TS = 38, CS = 19, PS = 57), with percentages of units within each class shown above each bar. RS and FS waveforms were mainly orientation-selective with 94% and 93% oriented RFs (RS = 59% SRFs, 35% MRFs; FS = 63% SRFs, 30% MRFs), respectively, and low proportions of non-oriented RFs (RS = 6% blob RFs; FS = 7% blob RFs). TS and CS waveforms were a mixture of oriented and non-oriented RFs (TS waveforms: 55% were blob RFs, while 45% were oriented; CS waveforms: 58% were blob RFs and 42% oriented). PS waveforms were mostly non-oriented: 84% blob RFs. The average OB for each spike waveform class was: 0.56 ± 0.19 for RS waveforms; 0.55 ± 0.21 for FS waveforms; 0.27 ± 0.23 for TS waveforms; 0.26 ± 0.25 for CS waveforms; and 0.14 ± 0.13 for PS waveforms. In general, RS and FS waveforms most closely align with oriented RFs, non-oriented filter types dominate PS waveforms, and TS and CS waveforms have an even mix of both.

Author Manuscript

This article is protected by copyright. All rights reserved.

The non-oriented receptive fields (blob RFs) have similar spatial structures to the centre-surround RFs observed in the thalamus (Cai *et al.*, 1997). Further, extracellular spike waveforms with large positive phases have been associated with recordings from axons in some studies (cat: Blanche et al., 2005, rat culture cells: Bakkum et al., 2013; Pan et al., 2014; Lewandowska et al., 2015). In our classification scheme units with large positive phases included PS, TS, and CS waveforms. We thus hypothesised that some of these units may be recordings from thalamic axons and, therefore, explored whether units with a high proportion of blob RFs (TS, CS and PS waveforms) might have other characteristics similar to those of thalamic neurons, as outlined in the section below.

Relationship of spike train statistics with WGN to waveform classes

We investigated several spike train statistics that are expected to differentiate between the response characteristics of visual cortical cells and thalamic cells. These include driven spike rate, response latency and 'burstiness' (Fig. 5). If units with some waveform classes were thalamic in origin, then they should provide thalamic-like response characteristics. We investigated this using the population of units for which we were able to characterise RFs using NIM as this gave the most thorough description of the RF (n = 325).

First, thalamic cells generally have higher spike rates than cortical cells (Bullier *et al.*, 1982). PS waveforms had the highest average driven spike rates of all waveform classes (4.1 ± 4.9 spks/s; Fig. 5A). Their spike rates were significantly higher than RS (2.5 ± 2.7 spks/s, t-test: $p = 0.004$) and FS waveforms (2.1 ± 2.0 spks/s, t-test: $p = 10^{-4}$) but not significantly higher than TS (2.7 ± 2.9 spks/s, t-test: $p = 0.1$) and CS waveforms (3.2 ± 2.2 spks/s, t-test: $p = 0.5$).

Second, due to the thalamus being positioned prior to the primary visual cortex in the visual pathway, thalamic cells usually respond earlier to visual stimuli than cortical cells. Figure 5B shows the population response latency from stimulus to response onset using the WGN stimulus. PS waveforms had an average response latency of 23.5 ± 11.2 ms, which was significantly shorter than RS (29.4 ± 6.7 ms, t-test: $p = 10^{-5}$) and FS waveforms (29.5 ± 4.2 ms, t-test: $p = 10^{-4}$). The 2-4 ms difference is consistent with the delays caused by monosynaptic connections between thalamic cells and cortical cells in cats (Reid & Alonso, 1995; Alonso *et al.*, 2001; Kara *et al.*, 2002). TS and CS waveforms had response latencies between those of PS and RS/FS waveforms, with average response latencies of 26.8 ± 6.1 ms and 26.5 ± 8.3 ms, respectively. TS waveforms had significantly shorter response latencies than RS (t-test, $p = 0.02$) and FS waveforms (t-test, $p = 0.004$), while CS waveforms had

This article is protected by copyright. All rights reserved.

Author Manuscript

significantly shorter latencies than FS waveforms (t-test, $p = 0.02$). The lower response latency indicates that the processing of these units with large positive waveforms (PS, TS and somewhat CS) is occurring before the negative-dominant waveforms (RS and FS waveforms), similar to the bottom-up processing between the LGN and V1. It is important to note that even though several studies use response latencies of single-units to visual stimuli to study the hierarchical processing in the visual pathway (Schmolesky *et al.*, 1998; Bullier, 2001), other studies show simultaneous visual response latencies between anatomical areas (Ouellette & Casanova, 2006). The discrepancy between our data and other studies may be the differences in stimuli used to compute latencies, as latencies are known to depend on stimulus parameters – such as the 30 ms grey screen between each white noise stimulus, which produced a powerful onset response.

Third, thalamic cells are known to spike in short intervals (i.e. burst spikes) more frequently than cortical cells (Guido and Weyand, 1995). We calculated the burst index (Fig. 5C), which is the ratio of burst spikes over all spikes, and an indicator of how bursty a cell is (Wang *et al.*, 2006). PS waveforms had an average burst index of 0.26 ± 0.17, which was significantly higher than all of the other four waveform classes (RS = 0.08 ± 0.09, t-test: $p = 10^{-16}$; FS = 0.12 ± 0.08, t-test: $p = 10^{-10}$; TS = 0.16 ± 0.14, t-test: $p = 0.002$; CS = 0.12 ± 0.07, t-test: $p = 10^{-4}$). Note that this method was used previously for thalamic cells (Wang *et al.*, 2006). We also used another burst index used for cortical studies (Snider *et al.*, 1998) which produced similar results (i.e. burst index of PS waveforms was significantly higher than RS, FS and TS waveforms).

These findings show that relative to RS and FS waveforms, PS waveforms differ in several response characteristics, all of which are consistent with the hypothesis that PS waveforms have properties similar to those of thalamic cells: higher spike rates; shorter response latencies; and larger proportion of bursty spikes. For TS and CS waveforms, the results are not as clear when compared to RS and FS waveforms.

RF orientation selectivity recovered with drifting gratings

We also obtained the orientation selectivity from 633 units that responded significantly to drifting gratings (most of these also responded to the WGN stimulus: 333 units). Even though far more units were obtained with drifting gratings, a disadvantage of using these stimuli over WGN is that the drifting gratings were not optimised to the tuning preferences of each unit across the recording track. Instead, we attempted to use drifting gratings with spatial

This article is protected by copyright. All rights reserved.

Author Manuscript

frequencies that strongly drove most units in the track. In contrast, WGN contains roughly equal power at all spatial frequencies (up to a cut off) and the optimal spatial frequency can be estimated post hoc through the NIM fitting procedure.

Figure 6A shows example orientation tuning curves of non-orientation selective units (upper two) and orientation selective units (lower two) measured with 16 differently oriented gratings. Figure 6B shows the distribution of OB values as a histogram. Twenty-seven percent of units were non-oriented (n = 172/633, OB < 0.2) and 73% oriented (n = 461/633, OB > 0.2). As with WGN, the distribution of OB values obtained from drifting gratings was bimodal with a trough near OB = 0.2, but unlike with the WGN data it was not significantly different from unimodality (Hartigan's dip test, p = 0.16). This was also the case in Gharat and Baker (2017), who suggested that the lack of bimodality is likely caused by the more discrete orientation tuning curves (16 for drifting gratings compared to 200 for WGN RFs).

Figure 6C is a bar graph showing the number of RF types for each spike waveform type (with percentages of units within each class shown above each bar). RS and FS waveforms were mainly orientation-selective with 82% and 89% oriented RFs, respectively, and low proportions of non-oriented RFs (RS = 18%; FS = 11%). TS and CS waveforms were a mixture of oriented and non-oriented RFs (TS waveforms: 38% non-oriented RFs, while 62% oriented; CS waveforms: 48% were blob RFs and 52% oriented). PS waveforms were mostly non-oriented: 81% non-oriented RFs. This shows the same alignment of waveform type and RF type as the WGN data.

We also compared units with the OB obtained from both WGN and drifting gratings (n = 214), shown as a scatter plot in Figure 6D. The correlation coefficient is 0.60, showing a strong positive linear correlation, and an 81% match in the same RF type (i.e. non-oriented type with OB < 0.2 and oriented type with OB > 0.2) between the WGN OB and drifting gratings OB.

Cortical silencing using muscimol

To test more directly the hypothesis that some unit waveforms, such as PS waveforms, are recordings of LGN axons, we performed experiments to silence cortical spiking using the GABA agonist muscimol. Topical application of muscimol is known to heavily supress local cortical activity through GABAergic inhibition via receptors on dendrites but has no direct effect on thalamocortical axons. Muscimol has been used extensively to study

Author Manuscript

This article is protected by copyright. All rights reserved.

thalamocortical afferents in the cortex (cat visual cortex: Jin et al., 2008; Vidyasagar et al., 2015, ferret visual cortex: Chapman *et al.*, 1991; rat hippocampus: Robbins et al., 2013). We recorded from the primary visual cortex before, during and after two topical applications of muscimol in each of three penetrations in three hemispheres of two cats. We expected that RS and FS waveforms would be completely suppressed after the application of muscimol as they are likely to be cells with their somas and dendrites residing in the visual cortex. On the other hand, we expected that most PS waveforms and some TS and CS waveforms would continue to spike after application of muscimol, as they are likely thalamic afferents.

We recorded from 146 SUs using this protocol. Figure 7A shows the distribution of these units for each waveform class in this population, before and after silencing. For each class, the number of units pre-muscimol (i.e. in the unsilenced cortex) is shown on the left and the number of units post-muscimol (i.e. in the silenced cortex) is shown on the right. A SU was considered to exist in the unsilenced or silenced cortex if the ratio of the number of spikes over all spikes in that state is greater than 0.1 (i.e. spikes in that state / spikes total > 0.1). All spiking activity from RS (n = 65/65) and FS waveforms (n = 11/11) was suppressed post-muscimol. Amongst CS waveforms, 15/17 units were suppressed post-muscimol. On the other hand, spiking activity continued in the majority of TS and PS waveforms in the silenced cortex (TS: n = 18/24 = 75%; PS: n = 11/10 = 110%). Interestingly, out of the 146 SUs recorded, only 127 of these SUs were recorded prior to silencing. For the remaining 19 SUs (12 TS, 1 CS and 6 PS waveforms) spiking behaviour only appeared post-muscimol (which explains the 110% for PS waveforms). These units could have appeared because natural brain movement brought them into the vicinity of a recording electrode, although this never happened for RS/FS units. Alternatively, they may represent examples of disinhibition via corticothalamic or corticocortical feedback circuits. For simplicity, we will be referring to the muscimol-affected cortex as the silenced cortex.

Figure 7B visualises the effect of muscimol application on the spiking activity of 41 SUs recorded from one MEA penetration. Note that the unit numbers do not correlate with electrode position as more than one SU was often recorded on channels. The deepest recording in this track was 2.9 mm below the surface. The unsilenced state of the cortex is represented before the first application of muscimol (M1), and the silenced state of the cortex is represented after the second application of muscimol (M2). Each row represents each SU's spiking activity plotted as a histogram over time (minutes). The figure shows that after the application of muscimol, only PS (black) and TS (purple) units remain. All the units that

This article is protected by copyright. All rights reserved.

Author Manuscript

remained (#10, #16, #33, #35 and #37) responded intermittently during the period of measurement, with extended periods of both activity and relative inactivity both before and after silencing. Units #20 and #38 only showed spiking after the second application of muscimol and not before. The plot also shows the spatial effect of muscimol. Units are ordered from most superficial (Unit #1) to deepest (Unit #41). The responses of units closest to the surface disappeared immediately after the first muscimol application (Units 1-13), while the loss of spiking took longer in the deeper channels. This shows the effect of muscimol diffusion as it progresses through the brain into the deeper layers of the cortex. The maximum disappearance time for the deep layers of RS and FS waveforms was approximately 20 minutes after the first application of muscimol.

These results indicate that all PS and most TS waveforms were not silenced by muscimol application and therefore are likely to be afferent or efferent axons from outside V1.

Receptive fields with muscimol application

White Gaussian Noise

We were able to successfully recover the spatial RFs of 41/146 SUs during the muscimol protocol using NIM and WGN. Figure 7C shows the population of units with oriented (blue, OB > 0.2) and non-oriented RFs (yellow, OB < 0.2) recovered in the unsilenced (left bar) and silenced cortex (right bar). Eleven units with oriented RFs were recovered in the unsilenced cortex while only two were recovered in the silenced cortex. Note that one of the oriented RFs recovered in the silenced cortex was non-oriented in the unsilenced cortex (details below; 6D.c). Out of the non-oriented RFs, 14 were recovered in the unsilenced cortex while 23 non-oriented RFs were recovered in the silenced cortex (7 of which existed in the unsilenced cortex).

Figure 7D visualises these RF units by plotting their orientation bias values in the silenced and unsilenced cortex. An OB of zero indicates that the RF did not exist in that state (i.e. the blue and yellow regions), either by having reduced spikes (<10% of the SU's total spikes) or insignificant RFs. This means that units residing in the white region of Figure 7D had a RF in both the unsilenced and silenced cortex (n = 9). Many of these units were non-oriented and remained non-oriented after muscimol application (67%, n = 6/9, bottom-left quadrant in Fig. 7D). They were all TS (n = 3) or PS waveforms (n = 3). An example is shown in Figure 7Fi, which shows the same non-oriented RF and spike waveform in both the unsilenced (left) and silenced (right) states of the cortex. The remaining three units were either characterised as

This article is protected by copyright. All rights reserved.

Author Manuscript

non-oriented, which was then characterised as oriented (top-left quadrant; n = 1; Fig. 7D.b), oriented that became non-oriented (bottom-right quadrant, n = 1; Fig. 7D.c), or oriented that stayed oriented (top-right quadrant, n = 1; Fig 7D.d). Note that the last two had noisy RF filters, which produces an ambiguous classification for orientation tuning. An example is shown in Figure 7D.c where the RF recovered in the unsilenced cortex (left) was classified as oriented with a near identical blob-shape RF recovered in the silenced cortex (right).

For units with a recovered RF only in the unsilenced cortex (n = 16; blue area in Fig. 7F), 9 were oriented and 7 were non-oriented. Three of these units were RS waveforms (19%), three were FS waveforms (19%), six were TS waveforms (37%), and four were PS waveforms (25%). An example RS waveform with its spike waveform and RF is shown in Figure 7F.e, which clearly shows an oriented RF in the unsilenced cortex (left) and a non-existent RF in the silenced cortex (right).

For units with a recovered RF only in the silenced cortex (n = 16; yellow area in Fig. 7D), all were non-oriented. Twelve of these units were TS waveforms (75%) and four were PS waveforms (25%). An example TS waveform with its spike waveform and RF is shown in Figure 7F.f.

Drifting gratings

A total of 114/146 SUs responded to drifting gratings during the muscimol protocol. Unlike the white Gaussian noise stimulus, we were only able to use gratings at fixed times relative to the muscimol protocol. Figures 7E and 7F are in the exact same format as in the WGN section (Fig. 7C and 7D). Out of the oriented RFs, 78 were recovered in the unsilenced cortex while only 3 were recovered in the silenced cortex. Out of the non-oriented RFs, 20 were recovered in the unsilenced cortex while 16 non-oriented RFs were recovered in the silenced cortex.

Out of the 92 units that only responded to gratings in the unsilenced cortex (illustrated in the blue region of Fig. 7F), the majority had oriented RFs (82%, n = 75/92) or RS waveforms (RS = 60%; FS = 8%; TS = 19%; CS = 10%; PS = 3%). An example is shown in Figure 7F.a, illustrating an RS waveform with an oriented RF in the unsilenced cortex (left) and a non-existent RF in the silenced cortex (right).

Six units responded to gratings in both the unsilenced and silenced cortex (white region in Fig. 7F). Three of these were non-oriented and remained non-oriented after muscimol

This article is protected by copyright. All rights reserved.

Author Manuscript

application (n = 3/6, bottom-left quadrant in Fig. 7F), which were TS (n = 2) or PS waveforms (n = 1). An example shown in Figure 7F.b, illustrating the same non-oriented RF and spike waveform in both the unsilenced and silenced states of the cortex. The remaining three units were characterised as oriented in the unsilenced cortex and then characterised as non-oriented in the silenced cortex (bottom-right quadrant), which were also TS or PS waveforms.

Out of the 13 units that responded to gratings only in the silenced cortex (yellow region in Fig. 7F), 10 were non-oriented and only 3 were oriented. They were either PS waveforms (n = 8, 62%) or TS waveforms (n = 5, 38%). An example is shown in Figure 7F.c, which clearly shows a non-existent RF in the unsilenced cortex (left) and a non-oriented RF with a PS waveform in the silenced cortex (right).

In summary, this analysis shows that recording in the silenced primary visual cortex revealed a high proportion of TS and PS waveforms that had RFs that were non-oriented. Furthermore, muscimol did not significantly affect the orientation selectiveness of cells that continued to spike in the cortically silenced state.

Characterisation of nonlinearity

Taking our population of RF units as characterised with WGN and the NIM, which also responded to drifting gratings (n = 246; n RS = 101, FS = 67, TS = 27, CS = 14, PS = 37), we characterised their nonlinearities based on four indices. (1) The F1/F0 ratio, which is commonly used to define V1 cells into simple or complex (Skottun *et al.*, 1991). (2) The F2/F1 ratio, which is commonly used to define LGN cells into X- or Y-cells (Hochstein & Shapley, 1976). Note that we calculate the F2/F1 ratio from drifting gratings instead of contrast reversing gratings (Hochstein & Shapley, 1976), which is still an indicator of linearity/nonlinearity but does not necessarily indicate X/Y type. (3) The symmetry index (SI; Eq. 5), obtained from the input nonlinearities of the NIM, which indicates a neuron's sensitivity to brightness polarity (Almasi *et al.*, 2020). (4) The number of spatial filters, which is an indication of spatial summation. Figure 8A-D plots all four indices for each waveform type, with the nonlinearity characterised as either linear (dark bars; $F1/F0 > 1$, $F2/F1 < 1$, $SI < 0$, nFilters = 1) or nonlinear (light bars; $F1/F0 < 0$, $F2/F1 > 1$, $SI > 0$, nFilters > 1).

Author Manuscript

This article is protected by copyright. All rights reserved.

Figure 8A suggests that RS waveforms, with 73% of its population categorised as complex cells, are more nonlinear than FS waveforms, with only 54% of its population categorised as complex. This is also supported in the symmetry index (RS = 57% nonlinear, FS = 42% nonlinear, Fig. 8C), but not in the number of filters (RS = 64% nonlinear, FS = 66% nonlinear, Fig. 8D).

Figure 8B illustrates that TS waveforms and PS waveforms, which may be recordings from thalamic axons, are dominated by linear characteristics (93% and 92% with F2/F1 < 1, respectively). This linear characteristic is also confirmed in the SI (Fig. 8C), where TS and PS waveforms had 74% and 97% of units with negative symmetry indices, respectively, and in the number of spatial filters (Fig. 8D) where TS and PS waveforms had 70% and 86% of units with only one spatial filter, respectively.

Conversely, the plots also show that CS waveforms, which are also mostly non-oriented, are dominated by nonlinear characteristics. The F1/F0 ratio, SI and number of filters indicate that 100%, 79% and 71% of CS waveforms are nonlinear, respectively. However, the result is not as powerful for the F2/F1 ratio, as only 29% of CS waveforms had nonlinear properties.

The results show reasonable correlation between the nonlinearity indices, with all revealing a strong dominance of linear properties for TS and PS waveforms, and three revealing a strong dominance of nonlinear properties for CS waveforms.

Author Manuscript

This article is protected by copyright. All rights reserved.

Discussion

Do classes of extracellular spikes correlate with spatial receptive field (RF) types in cat V1 (Area 17/18)? We categorised spikes into five extracellular waveform classes: regular-spiking (RS), fast-spiking (FS), triphasic-spiking (TS), compound-spiking (CS), and positive-spiking (PS). RFs were estimated using drifting sinusoidal gratings and white Gaussian noise (WGN) with the nonlinear input model (NIM). Both techniques revealed units with either oriented or non-oriented RF types. Nearly all RS and FS waveforms exhibited oriented RFs, PS waveforms had overwhelmingly non-oriented RFs, and TS and CS waveforms were a mixture of the two. These findings, along with other diagnostic spiking characteristics, reveal that some of the TS and CS waveforms, and most of the PS waveforms have properties similar to dLGN neurons. To test this hypothesis, we recorded from muscimol-affected (i.e. silenced) visual cortex and discovered that spiking activity only continued in PS and TS waveforms, suggesting that these units are recordings from axons originating from outside V1. Our findings strongly suggest that most PS waveforms and some TS waveforms are recordings from afferent axons of the dLGN.

Biophysics of extracellular spike waveform classes

The negative trough followed by a prolonged positive-going phase in RS/FS waveforms is generated by the opening and closing of sodium and potassium channels, respectively (Henze *et al.*, 2000). In rodents, the difference in spike duration between regular- and fast-spiking neurons are likely due to the difference in expression levels of Na+ and K+ channels (Martina & Jonas, 1997; Martina *et al.*, 1998). The shorter durations of fast-spiking neurons are due to the faster repolarisations of Kv1 and Kv3 channels. However, this may not be clear-cut as studies have found the presence of these channels in macaque pyramidal neurons (Ichinohe *et al.*, 2004; Constantinople *et al.*, 2009). The initial dominant negative troughs suggest that RS and FS waveforms are recordings made close to somas (Gold *et al.*, 2006). Broad extracellular waveforms have been associated with pyramidal and spiny stellate neurons (excitatory neurons), while narrow extracellular waveforms have been associated with basket and chandelier interneurons (GABAergic inhibitory neurons) (Barthó *et al.*, 2004). However, recent studies in monkey cortex showed pyramidal cells exhibiting narrow-waveform spikes (Vigneswaran *et al.*, 2011; Onorato *et al.*, 2019) and GABAergic neurons in mice cortex with broad action potentials (Gentet *et al.*, 2010), which indicates that the associations between spike duration and cell type classification may not be definitive. Therefore, it is important to

Author Manuscript

This article is protected by copyright. All rights reserved.

note that our broad spikes (RS waveforms) and narrow spikes (FS) are not necessarily associated with excitatory and inhibitory neurons, respectively.

Compared to RS and FS waveforms, TS, CS and PS waveforms have a significant positive peak possibly due to a mixed-ion capacitive current that becomes more profound as the recording electrode is placed more distal from the soma (Gold *et al.*, 2006). The peak may arise from recordings made distal to the soma: either dendritic spikes (monkey V1: Gur et al., 1999; rat cortex: Henze et al., 2000; Jia et al., 2019, cat cortex: Gold et al., 2009, monkey retina: Petrusca et al., 2007) or axonal spikes (cat: Blanche et al., 2005, rat cortex: Raastad and Shepherd, 2003; Robbins et al., 2013, cultured rat cortical cells: Bakkum et al., 2013; Pan et al., 2014; Lewandowska et al., 2015; monkey retina: Petrusca et al., 2007). This is also predicted in models of current source and sink from extracellular spikes that propagate through an isolated axon; likely due to the variation in morphology and ion channels (Heinricher, 2004; Barry, 2015). Slow spikes with significantly lower amplitudes, as seen in CS waveforms, have been theorised to occur when the distance between the recording site and the soma is large due to the contribution from distal sources to the action potential (Heinricher, 2004; Gold *et al.*, 2006). It is important to note that the positive-spiking dendritic studies mentioned above reported smaller signals (~20 μV) than the PS waveforms in this study (~100 μV). Larger extracellular positive spikes (>500 μV) have been recorded previously in cat visual cortex (named high-amplitude positive spikes, HAPS), which were orientation-selective (Gold *et al.*, 2009). Our unit population is unlikely to contain HAPS as none of the PS waveforms exceeded 250 μV and most were non-oriented.

Receptive field abundance

Why did only 38% (n = 325/855) of SUs exhibit RFs when using the NIM? (1) We used WGN because it is the most general stimulus possible but, of course, it has few high contrasts and many low contrasts. The recovery of RFs exclusively depended on each neuron's responsiveness to WGN stimuli, and many units did not respond well to the WGN. (2) Even though 442 units (52%) were responsive to WGN, in many cases (n = 117) we were unable to extract significant RFs. In fact, we recovered traces of RF from many more units, but they were not statistically significant. We set a strict threshold for significance, as revealed by the clean spatial RFs (e.g. Fig. 4), which have little to no background noise. (3) For some units, it was difficult to extract enough spikes during the recording period (approximately 2 hours), due to factors such as spikes changing shape due to brain movements, which led us to

Author Manuscript

This article is protected by copyright. All rights reserved.

discount the data. (4) There are neurons in the visual cortex that do not respond reliably to visual stimuli: 13% in the current study; 23% in mice (Vries *et al.*, 2020). This is a relatively recent finding likely due to the different sampling bias of MEAs compared to single-electrode recordings. These neurons could be cells that are unresponsive to monocular stimuli (Pettigrew *et al.*, 1968), or possibly involved in non-visual computation (Stringer *et al.*, 2019), multisensory processing (Cappe *et al.*, 2009), or only be responsive to specific natural features as a result of hierarchical processing (Yosinski *et al.*, 2015).

On average, we obtained 40 sorted SUs per penetration from 32 electrodes. It is important to note that our total time of recording per penetration is long with a median recording time of 8.0 hours (min = 3 hours, max = 28 hours). We found that during these long recordings, some spikes only lasted for a few hours and others often replaced them over time. We carefully tracked these appearances and disappearances and only correlated a given SU with stimuli presented during their existence. It was also common to have two clearly identifiable spikes per electrode, which increased our SU count overall. Furthermore, despite the fact that Kilosort is designed to rectify the spatial issues from neural recordings (i.e. the same neuron recorded on multiple channels), and we were careful with our manual curation, it is possible that the neuronal population in this study contains the same neuron but with different waveforms, depending on the proximity of the recording site to different parts of the neuron (Gold *et al.*, 2006).

Non-oriented receptive fields

Classically, the majority of RFs from cat V1 (Area 17/18) have been defined as orientation selective (for review, see Van Hooser, 2007). Units with non-oriented RFs have sometimes been reported in cat visual cortex (~5%: Henry *et al.*, 1979; Bullier & Henry, 1979; Nowak *et al.*, 2008) and are often reported in macaque V1 (Hubel & Livingstone, 1981; Ringach, 2002; Ringach *et al.*, 2002, 2003). The current study in cat V1 recorded a higher proportion (relative to past studies) of non-oriented RFs (27-29% of units with OB < 0.2). With the advent of MEAs, non-oriented RFs have been reported more frequently in cat visual cortex: 40-43% non-oriented in cat Area 18 (Talebi & Baker, 2016; Gharat & Baker, 2017). We, and the authors mentioned above, speculate that the most probable reason for this recent observed increase is the adoption of MEAs, which provides a more objective sampling of the cortical space than single electrodes, and the systematic bias from using test stimuli in which neurons were identified in single-neuron electrophysiological recordings (Talebi & Baker, 2016;

This article is protected by copyright. All rights reserved.

Vries *et al.*, 2020). This was evident in Talebi & Baker (2016), as they compared the differences in receptive field type (oriented vs non-oriented) and electrode type (single vs multi), and found that their multi-channel electrodes yielded a much greater percentage of cells with non-oriented RFs than single-channel electrodes. We also think that the advancement of spike-sorting algorithms has helped with uncovering non-oriented RFs. The negative threshold crossings used for spike detection in traditional methods and algorithms would have bypassed any positive-spiking units, resulting in a decrease in the overall population of non-oriented RFs. We noticed this during our online data analysis where we did not observe many positive spiking waveforms or non-oriented RFs due to us using a negative threshold for spike detection. Only during post-processing did we notice an abundance of positive-spiking waveforms and non-oriented RFs. Therefore, the recent adoption of MEAs, the visual stimulus used and advancements in spike-sorting algorithms have most likely led to the influx of reported non-oriented RFs and positive-spiking units.

Using a generalised receptive field analysis, Talebi & Baker (2016) found that 43% of cat Area 18 units were non-orientation tuned. They classified the spikes associated with the recovered RFs and reported the spike waveforms as all having an initial negative trough and being either biphasic or triphasic. Cells were not divided into RS and FS types. They found no correlation between RF type and spike width. For those that could be analysed offline a measure of peak-to-valley time (maximum to its minimum) was used, without reporting the relative amplitude of the peak. Therefore, it is not possible to directly compare our spike waveforms with those reported by Talebi & Baker (2016). Gharat & Baker (2017) then did an analysis of cat Area 18 in which gratings were used as stimuli. They again found that 40% of units were non-oriented but did not present a population analysis of the spike waveforms. They did present six example spike waveforms for non-oriented Area 18 units. Of these, three (50%) would be classed as PS units in our analysis, one (16.7%) as a TS unit, and two as either RS or FS (33.3%). If these example cells are fully representative, the proportions correspond reasonably well with our findings, i.e. the great majority of non-oriented units are either PS or TS. A third of these non-oriented cells found in Gharat & Baker (2017) were binocular, which were unlikely to be LGN afferents and may explain their higher proportion of non-oriented cells compared to the current study. For the remaining two-thirds, they claim that these cells were unlikely to be LGN afferent fibres because they were found across all cortical depths. However, it is important to note that LGN cells (X, Y and W cells) projects to all layers of the cortex – although the proportion may differ (for review, see Alonso, 2002).

This article is protected by copyright. All rights reserved.

Author Manuscript

Muscimol and predictions on the origin of each spike class

The persistence of extracellular spiking units following cortical silencing has been reported previously and assumed to represent thalamocortical afferents (cat visual cortex: Jin et al., 2008; Vidyasagar et al., 2015, ferret visual cortex: Chapman *et al.*, 1991; rat hippocampus: Robbins et al., 2013). Muscimol was used in this study to determine which units would remain after cortical silencing. As muscimol specifically affects the GABA receptors in the dendrites of cortical cells, units silenced by muscimol are likely to have somas in the cortex while units unaffected by muscimol likely originate outside the cortex. Chapman *et al.* (1991) showed that responses from muscimol-silenced cortex (from one ferret) were of thalamocortical afferents by electrical stimulation of the LGN. Although not definitive, this section will discuss the most logical conclusions based on the muscimol protocol, in conjunction with the other results from this study and previous studies.

The complete muscimol-silencing of all RS and FS spikes, i.e. the biphasic spike waveforms with large, negative going initial phase and the oriented RFs and delayed responses, suggest that RS and FS waveforms are recordings from somas residing in V1. The low proportion of non-oriented RS and FS waveforms (6-7%, Fig. 4D) matches the proportion of non-oriented RFs in cat Area 17 studies using intracellular recording (~5%; Nowak *et al.*, 2008).

TS waveforms are likely recordings from a mixture of cells with local cortical- or thalamic-origins. This is evident in their even proportion of oriented and non-oriented RFs, shorter response latencies relative to RS/FS waveforms and some of TS waveforms persisting after muscimol application. For CS units, we cannot say with confidence where their somas originate due to their low numbers (7%). It could be argued that TS and CS waveforms are of the same spike class, as they have similar proportions of RF type and spiking characteristics. We left them separate due to the unusual shape, low amplitude, and slow waveform of CS units, which have not been described in depth before. Again, this may be because of the more objective sampling from MEAs and spike-sorting algorithms, where abnormal and low amplitude spikes can be extracted reliably.

PS waveforms are likely recordings of axons originating from the thalamus. First, the RFs of PS waveforms are mostly non-oriented (74-83%). This link between positive spikes and non-orientation selective cells has been made in macaque V1 (Gur *et al.*, 1999). They recorded small-amplitude positive spikes that were slightly less tuned to orientation (mean orientation bandwidth = 79°) than the negative spikes (mean orientation bandwidth = 40°), but more

This article is protected by copyright. All rights reserved.

Author Manuscript

selective to orientation than LGN cells and our PS waveforms (mean orientation bandwidth for WGN data = 152°; full width at half-maximum of the orientation tuning curve). Second, the spiking characteristics of PS waveforms were similar to thalamic cells: higher spike-rate (Bullier *et al.*, 1982); shorter response latencies (Kara *et al.*, 2002); higher proportion of burst responses (Guido & Weyand, 1995). Strong evidence that PS waveforms are from axons originating outside V1 is the muscimol experiment; the great majority of PS waveforms present before muscimol application were present after application. Together, these lines of evidence strongly support the view that PS waveforms are from axons originating in the dLGN.

This then asks the question: if PS waveforms were recordings of putative LGN axons, why were none (or virtually none) of the many axons of cortical cells detected? We can only speculate that the LGN axons detected in this study were larger than cortical axons. However, in truth we cannot answer this criticism at this time. Why did some extra PS and TS waveforms, usually with non-oriented RFs, appear after muscimol application? We propose the following theory. (1) The muscimol would silence excitatory cortical cells in layer 6 that feed back to the dLGN. (2) If these excitatory cortical cells drive inhibitory interneurons in the dLGN, which suppress feedforward pathways, the drive would stop after muscimol. (3) As a result, there might be disinhibition of thalamic feedforward neurons destined for V1. Of course, we cannot discount the possibility that these spikes appeared purely due to brain movement, but there was no evidence of other cell types randomly coming and going.

We also show that a high proportion of PS and TS waveforms with recovered RFs were characterised as linear using the F2/F1 ratio, symmetry index of the NIM input nonlinearities, and the number of spatial filters (PS = 86-97% nonlinear, TS = 70-93% nonlinear). Given that PS and TS waveforms are likely recordings from thalamic axons, then the analysis strongly indicates that they are both from LGN X-cells. It is possible that some of the TS waveforms could be W- or Y-cell afferents due to their slightly higher proportion of nonlinear units. The spikes associated with CS waveforms could also be from thalamic axons and the abundance of nonlinear CS waveforms indicates that some of our CS recordings may be of LGN Y-cell axons, cortical neurons that received direct input from those axons, or cortical neurons receiving input from two opposing X-cells (i.e. one ON and one OFF). It is possible that we were recording from the dendritic branches of those cortical neurons. Again, we cannot make a definite conclusion for CS units due to their low population.

Author Manuscript

This article is protected by copyright. All rights reserved.

Conclusion

Just as Niell and Stryker (2008) did for mouse, we have fully characterised the extracellular spike waveforms and RFs for cat V1 cells using both drifting gratings and WGN. We concur with Martinez *et al.* (2005) that simple and complex cells (or single- and multi-featured in the present study) are not correlated with particular cell types. However, we uncovered a sub-population of units with non-oriented RFs in V1, likely due to the different sampling bias of MEAs and advancement in spike-sorting algorithms, that are strongly associated with positive-spiking classes of waveforms. Putting the findings together, we suggest that positive-spiking waveform recordings in cat V1 may largely arise from the axons of dLGN input neurons. This would mean that future extracellular studies may need to consider the subpopulation of units recorded in V1, or even other brain regions, that do not originate from the targeted area. However, it does allow cortically implanted electrodes to record from V1 cortical neurons and dLGN afferents simultaneously. This in turn makes it easier for researchers to assess the feedforward connectivity between cortical V1 and its subcortical input, the dLGN.

Author Manuscript

This article is protected by copyright. All rights reserved.

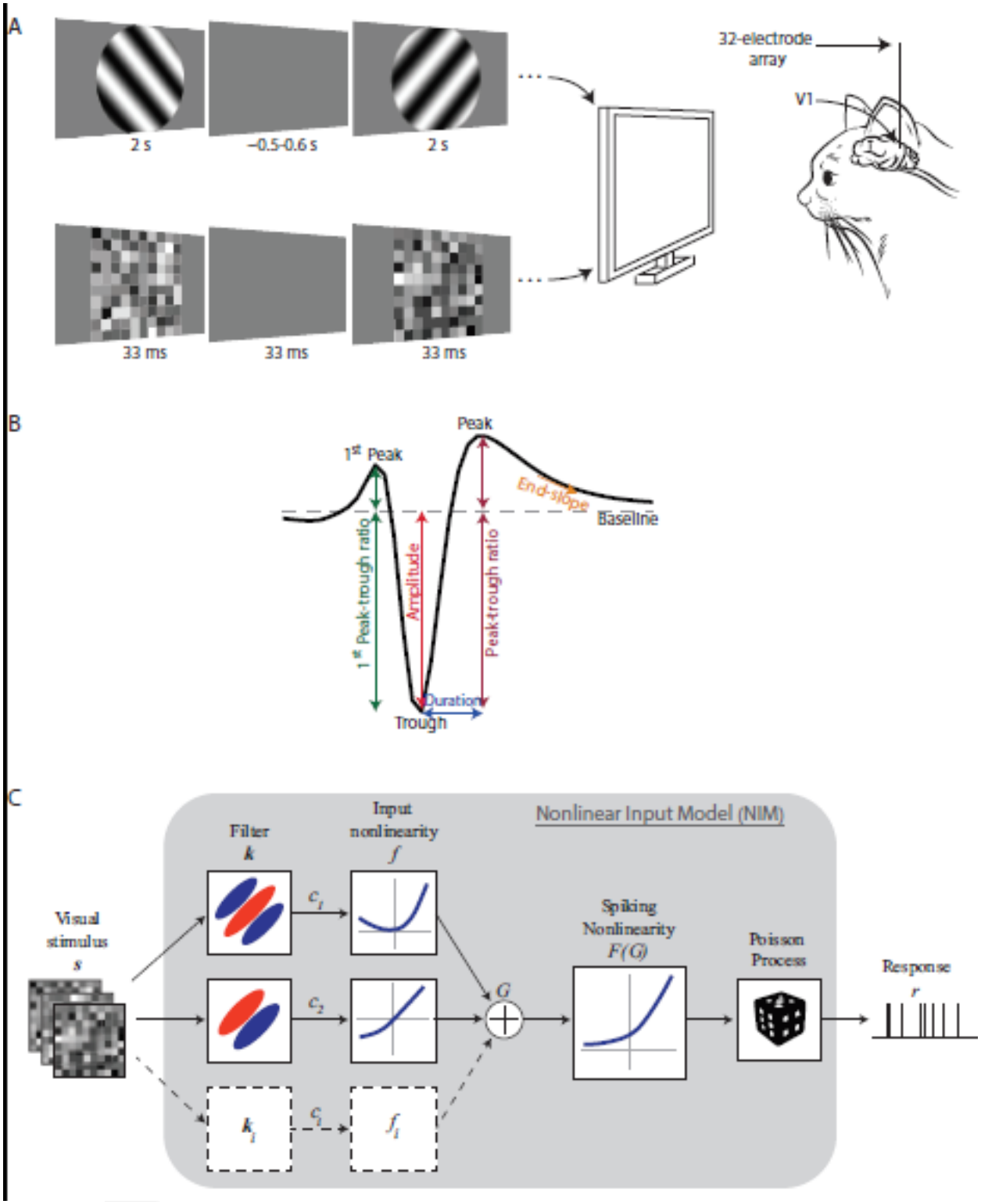


Figure 1. (A) Schematic of experimental and stimulus design. Two types of stimuli were used: drifting sinusoidal gratings and white-Gaussian noise (WGN). Gratings were presented in 16 different directions for 2 s (0.5 s static, 1 s drift, 0.5 s static) followed by a randomised 0.5-0.6 ms grey screen. Each direction was presented at least 5 times. WGN were presented

This article is protected by copyright. All rights reserved.

at 30 Hz, with a grey screen at equal presentation time after each WGN image, and presented in blocks of 12,000 images. Neural responses were recorded with a 32-electrode array in the cat primary visual cortex (Areas 17 and 18). **(B)** Example extracellular spike waveform with three major deflections (1st Peak, Trough and Peak) with the baseline shown as the dashed line. Spikes are classified based on five features: Amplitude is the difference between the maximum unsigned peak and the baseline; Peak-trough ratio is the ratio between the peak and trough; 1st Peak-trough (green) is the ratio between the 1st Peak and Trough; Duration is the time between the Trough and Peak; and End-slope is the gradient at time x after the Trough and Peak. The optimum value for time x is calculated in the Results section. **(C)** Schematic illustrating the nonlinear input model (NIM) based on physiological processes. In parallel streams, each spatial filter ($\boldsymbol{k}_i$) processes the visual stimulus ($\boldsymbol{s}$) resulting in the feature contrasts (c_i), which are then fed into the input nonlinearity (f). These parallel streams combine to produce the generator signal (G), processed by the parametric spiking nonlinearity ($F(G)$), and are finally randomised by a Poisson process to produce a response (r) for the neuron.

Author Manuscript

This article is protected by copyright. All rights reserved.

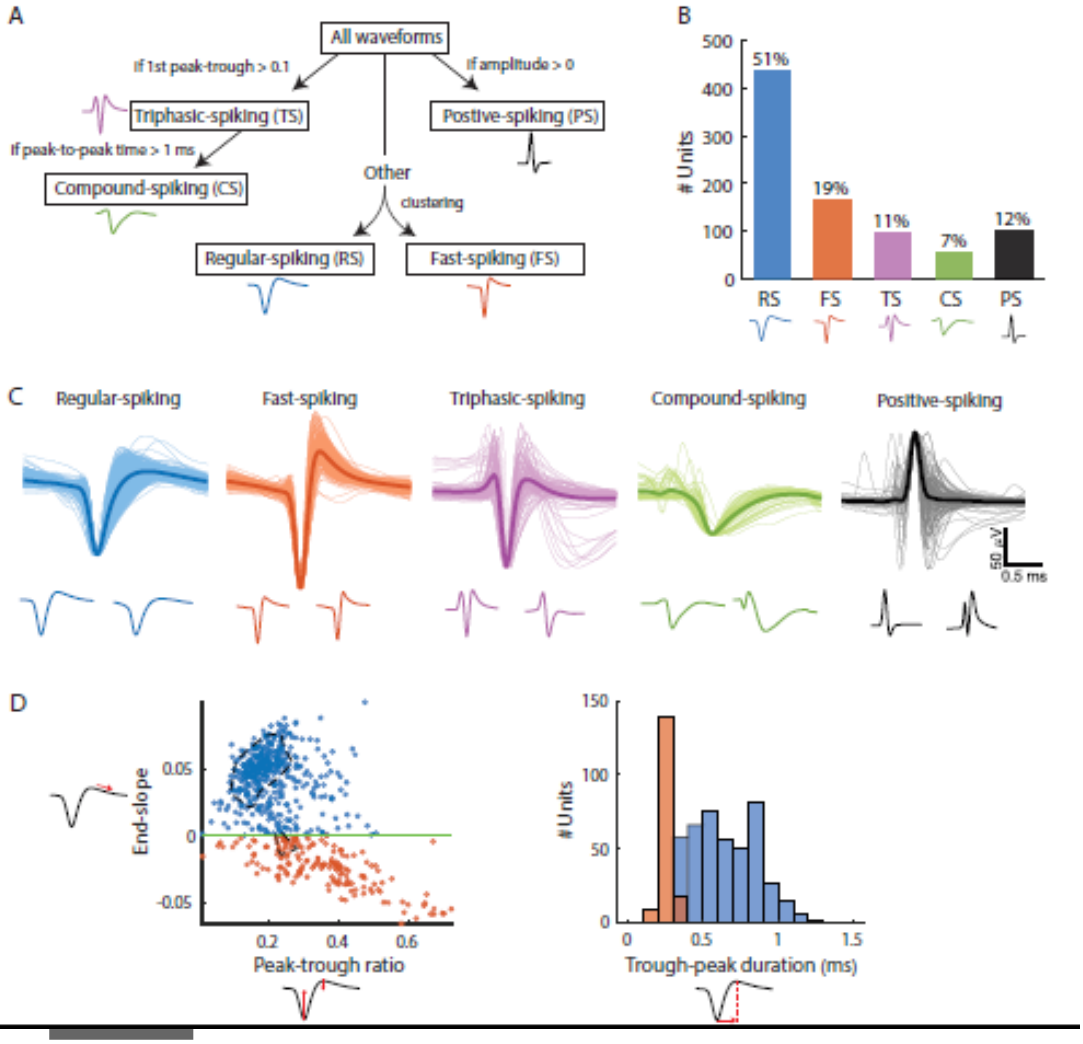


Figure 2. Characterisation of extracellular spike waveforms. For all plots: units with regular-spiking (RS, blue); fast-spiking (FS, orange); triphasic-spiking (TS, purple); compound-spiking (CS, green), and positive-spiking waveforms (PS, black). **(A)** Decision tree used in classifying extracellular spike waveforms. **(B)** Bar graph of population numbers for each waveform class in number of units. The percentages of each population out of all SUs are indicated above the bars. **(C)** Extracellular Spike waveforms separated by classification for all collected SUs. The lighter lines indicate the mean waveform for each SU and the darker lines indicate the overall mean for that group. RS, FS, TS, and CS waveforms are aligned and normalised to the trough. PS waveforms are aligned and normalised to the peak. Waveforms within each group are normalised by their overall mean amplitude. The bottom row illustrates two example SU waveforms from each group to show distribution. The scale bar on the right only applies for the top row. **(D)** Separation of RS and FS waveforms. Left: scatter plot of peak-trough ratio (X-axis) against end-slope (Y-axis). End-slope was measured as the gradient at 0.33 ms post-trough time. Separation was at end-slope = 0 as indicated by the green-line. The dashed black lines represent the area peaks > 10 when the X and Y axes are binned at 0.05 and 0.5 µV/sample, respectively. Right: histogram of trough-peak duration. The number of units (Y-axis) is reported in 0.1 ms bins.

`

This article is protected by copyright. All rights reserved.

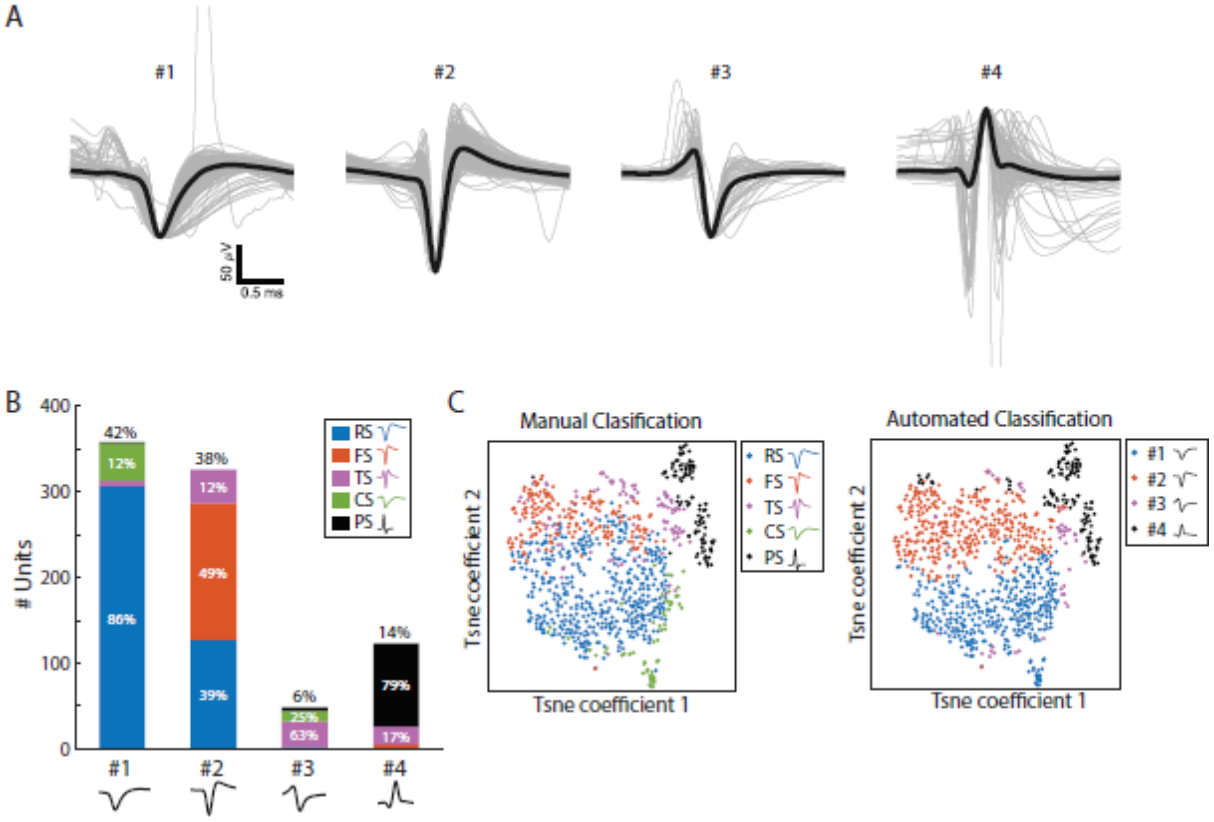


Figure 3. Characterisation of extracellular spike waveforms using the automated classifier. **(A)** Similar to Figure 2C, mean waveform for each SU for each waveform category (#1, #2, #3 and #4) from the automated classifier. The lighter traces indicate the mean waveform for each SU and the darker lines indicate the overall mean for that group. #1, #2 and #3 waveforms are aligned and normalised to the trough while #4 waveforms are aligned and normalised to the peak. **(B)** Bar graph showing the population numbers for each class with the percentages of each indicated above the bars. The proportion of classes with the manual classifier (as shown in Figure 2 – RS, blue; FS, orange; TS, purple; CS, green; and PS waveforms, black) are shown within each bar along with their percentages. **(C)** Visualisation of units using t-distributed stochastic neighbour embedding (t-SNE). Each data point corresponds to a SU coloured by waveform groups from the manual classifier (left) and from the automated classifier (right).

Author M

This article is protected by copyright. All rights reserved.

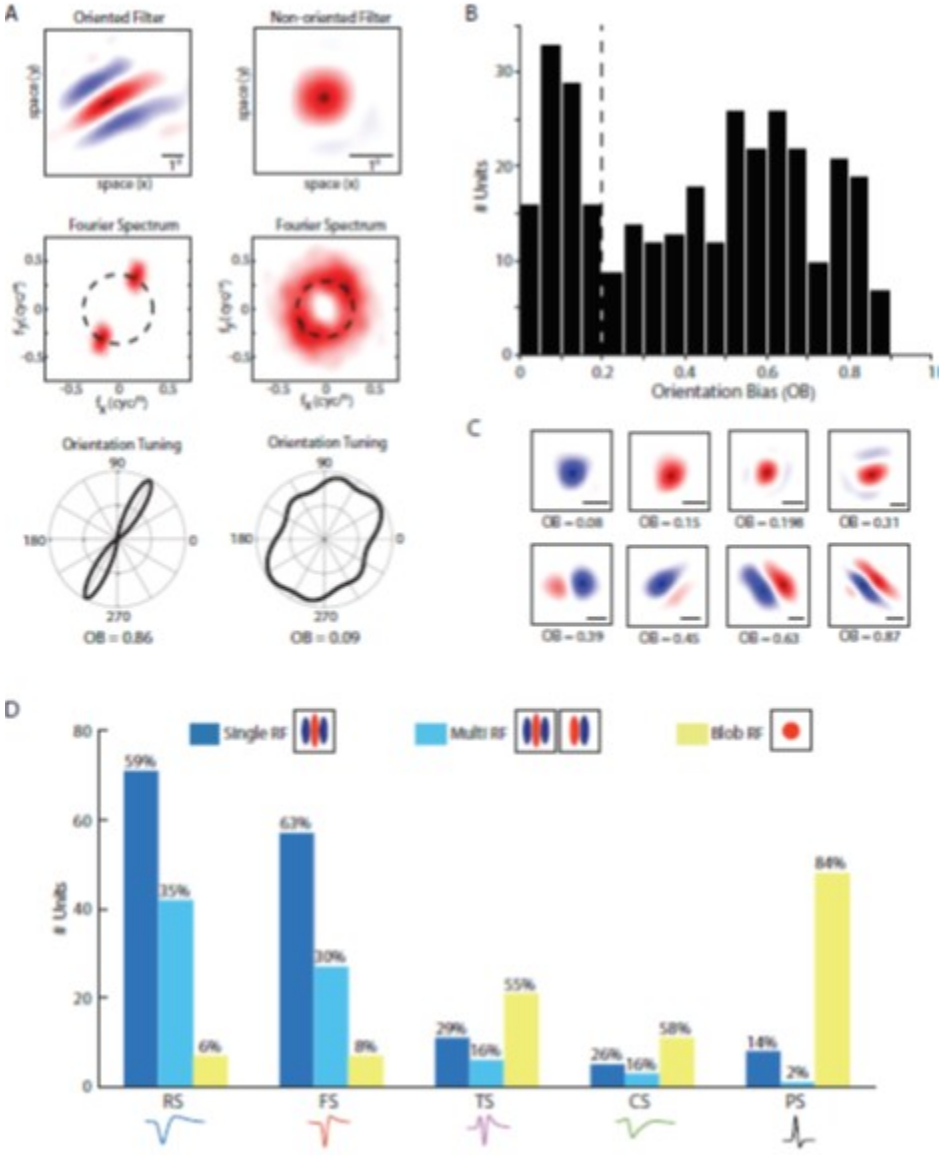


Figure 4. Receptive field characterisation using white Gaussian noise (n = 325). **(A)** Top row: example spatial receptive field filters from two SUs that were classified into either oriented (left column) or non-oriented (right column). Red indicates ON (responds to brightness increments) and blue indicates OFF (responds to brightness decrements). Middle row: The 2D Fourier transform of the spatial RFs (amplitude spectrum), and frequency shifted so that the spatial frequency components are symmetrical about the origin. The X and Y axes denote spatial frequency. The black dashed circle indicates the preferred spatial frequency of the filter. Bottom row: Orientation tuning plots of the filter obtained by sampling the amplitude spectrum at the preferred spatial frequency. From the orientation tuning curves, the orientation bias (OB) of RF A and filter RF B are 0.86 and 0.09, respectively. **(B)** Histogram of number of RF units by their orientation bias (OB), showing a

Author

This article is protected by copyright. All rights reserved.

binary distribution. Each bin shows the number of units with OB in steps of 0.05. RFs. OB > 0.2 were classified as oriented and RFs with OB < 0.2 were classified as non-oriented (indicated by the dashed black line). **(C)** Example spatial RFs with the same format as the top row of (A) and (B). The scale bar on the bottom-right of all RF plots indicates 1° of visual space. **(D)** Bar plot showing the population of waveform types and their RF types as number of units. The legend above shows the RF types: single-feature RF (SRFs, dark blue) have one oriented filter, multi-feature receptive fields (MRFs, light blue) are oriented with more than one filter, and non-oriented RFs (blob RFs, yellow). The X-axis represents the different waveform types. The percentages above each bar indicate the proportion of RF types within that waveform class.

Author Manuscript

This article is protected by copyright. All rights reserved.

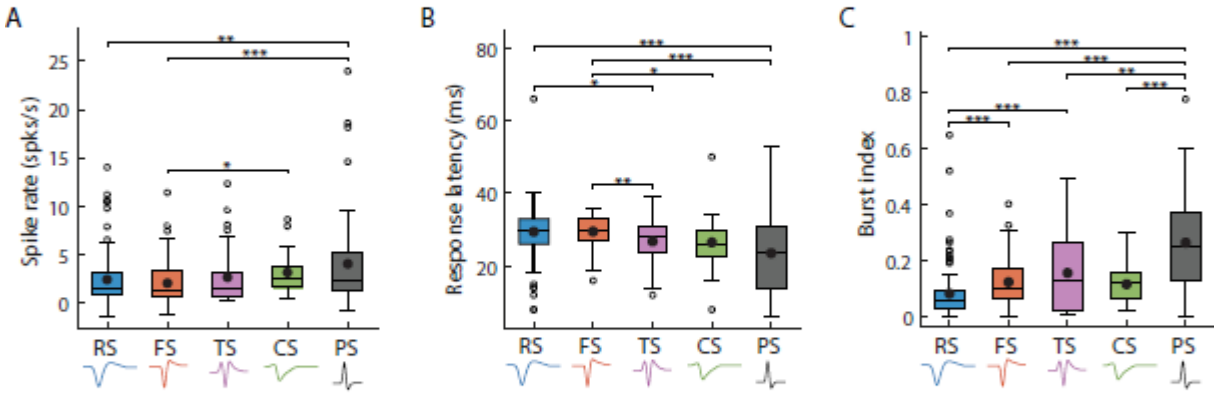


Figure 5. Box plots of RF units' (n = 325) spiking characteristics in response to WGN, categorised by their waveform type. **(A)** Driven spike-rate measured in spikes per second with the spontaneous subtracted. **(B)** Visual response latency which describes the time (ms) the unit responds after the WGN stimulus is presented. **(C)** Burst index which is the ratio of burst spikes over all spikes. The line dividing each box represents the median, he solid black circle represents the mean, the box represents the middle 50% of scores for the group, and the empty circles indicate the outliers. *, ** and *** represent $p < 0.05$, $p < 0.01$ and $p < 0.001$ (t-test), respectively.

Author MV

This article is protected by copyright. All rights reserved.

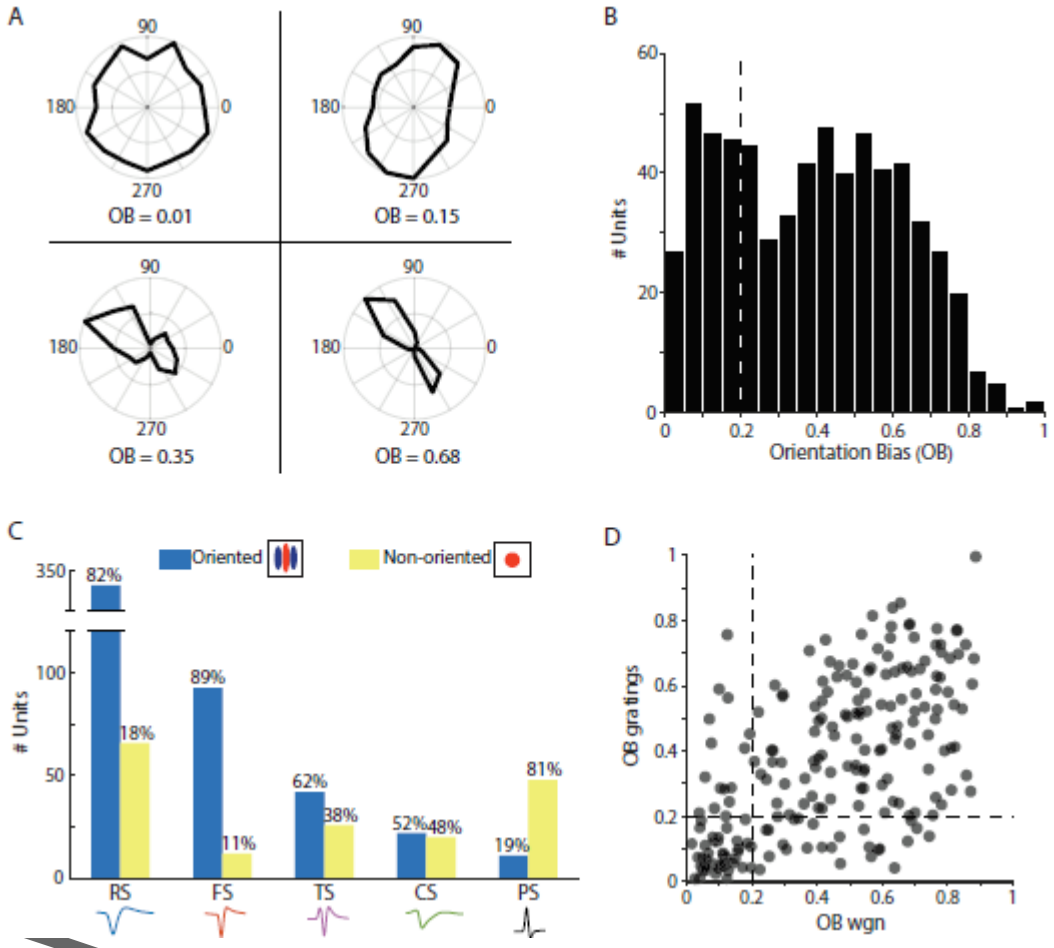


Figure 6. Receptive field orientation selectivity characterisation using drifting gratings (n = 633). **(A)** Example orientation tuning plots of non-oriented RFs (left two) and oriented RFs (right two). The smaller circle within represents half-maximum. **(B)** Histogram of number of units by their orientation bias (OB) in the same format as Figure 4B. **(C)** Bar plot showing the population of waveform types and their RF types in a similar format as Figure 4D but with only two RF types: oriented RF (blue) and non-oriented RFs (yellow). The X-axis represents the different waveform types. The percentages above each bar indicate the proportion of RF types within that waveform class. **(D)** Scatter plot comparing the OB obtained from both WGN and gratings data (n = 214).

Author M

This article is protected by copyright. All rights reserved.

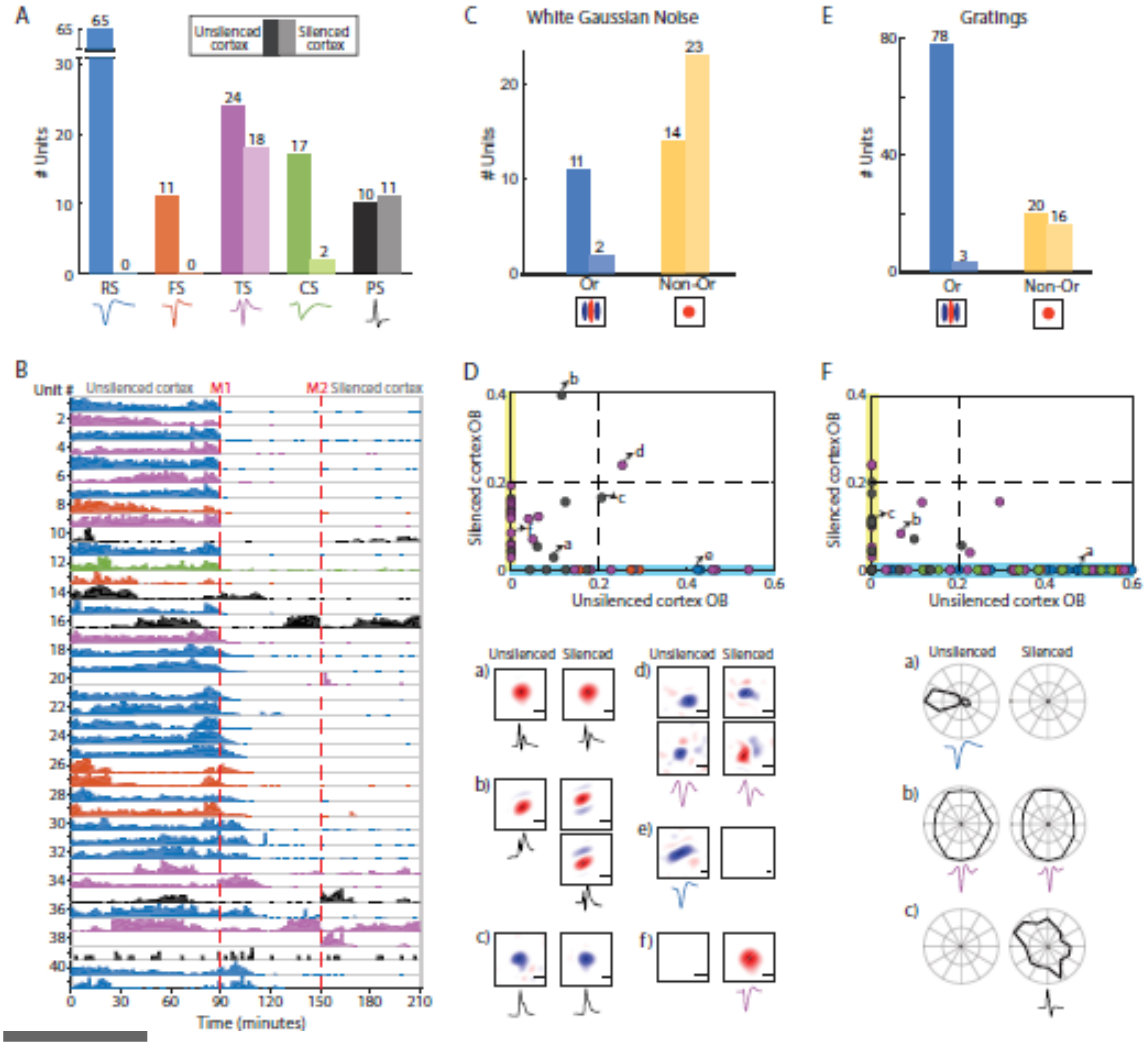


Figure 7. Effect of muscimol application on cortical activity and RF classes. **(A)** Population statistics for all SUs recorded with the muscimol protocol (n = 146). Bars indicate the number of units for each waveform class with the darker (left) and lighter bars (right) indicating the number of units in the unsilenced and muscimol-applied (i.e. silenced) cortex, respectively. The n values are indicated above each bar. A SU was counted in the silenced or unsilenced state if the ratio of number of spikes in that state / total spikes > 0.1. **(B)** Visual representation of the effect of muscimol over time (one penetration track, n = 41). Each SU is represented in each row of the plot and organised in depth (top is closest to the surface). Within each row are the spikes of the SU displayed as a histogram of number of spikes collected in 2-minute bins. The two dashed red lines (M1 and M2) represent the two applications of muscimol. Time 0 to M1 represents the unsilenced cortex, and time M2 to the end represents the

Author

This article is protected by copyright. All rights reserved.

silenced cortex. **(C-F)** RF types obtained from WGN (C-D; n = 41) or drifting gratings (E-F; n = 114) of SUs during the muscimol protocol. **(C, E)** Using the same format as in A, we show the oriented and non-oriented unit numbers before and after muscimol application. **(D, F)** Scatter plot of units with characterised RFs with the silencing protocol as orientation bias (OB) of RFs in the unsilenced (x-axis) and silenced cortex (y-axis). The dashed black lines indicate OB = 0.2 as it was used to classify oriented RFs (OB > 0.2) and non-oriented RFs (OB < 0.2). An OB of zero indicates that a RF did not exist in that state due to unresponsiveness (< 10% spikes overall) or insignificant spatial RF. This means that units lying in the shaded blue area (on the x-axis) had a RF only in the unsilenced cortex, units in the shaded yellow area (on the y-axis) had a RF only in the silenced cortex, and units in the white region had a RF in both the unsilenced and silenced cortex. Some overlapping data points were jittered for visualisation purposes. **(D a-f, F a-c)** RF and mean waveform in the unsilenced (left) and silenced cortex (right) of example units. The scale bars in the bottom-right of the spatial RFs indicate 1° of visual space. Blue = RS waveforms, orange = FS waveforms, purple = TS waveforms, green = CS waveforms, and black = PS waveforms for all plots with waveform data.

Author Manuscript

This article is protected by copyright. All rights reserved.

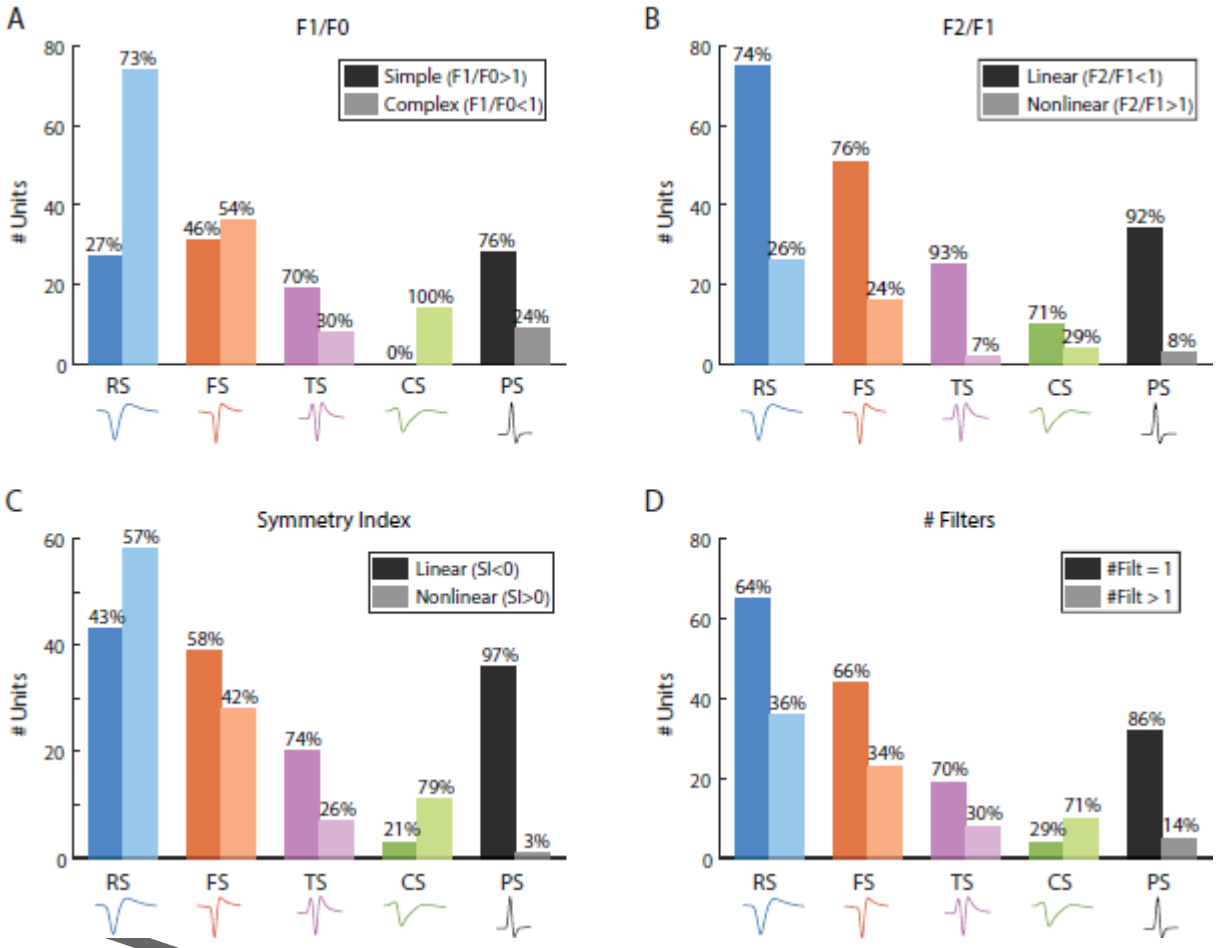


Figure 8. Characterisation of RF units' nonlinearity separated by their waveform classification using four methods: **(A)** F1/F0 ratio; **(B)** F2/F1 ratio; **(C)** symmetry index (SI); and **(D)** number of spatial filters. Only units with a recovered RF that also responded to drifting gratings were considered (n = 246). The legend in each plot shows the nonlinearity types. Linear types are shown as dark bars and nonlinear types are shown as light bars for all plots. The percentages above each bar indicate the proportion of nonlinearity types within that waveform class.

Author Manuscript

This article is protected by copyright. All rights reserved.

References

Akansu AN, Haddad PA, Haddad RA & Haddad PR (2001). *Multiresolution Signal Decomposition: Transforms, Subbands, and Wavelets*. Academic Press.

Almasi A, Meffin H, Cloherty SL, Wong Y, Yunzab M & Ibbotson MR (2020). Mechanisms of Feature Selectivity and Invariance in Primary Visual Cortex. *Cereb Cortex* **30,** 5067–5087.

Alonso J-M (2002). Book Review: Neural Connections and Receptive Field Properties in the Primary Visual Cortex. *The Neuroscientist : a review journal bringing neurobiology, neurology and psychiatry* **8,** 443–456.

Alonso J-M, Usrey WM & Reid RC (2001). Rules of Connectivity between Geniculate Cells and Simple Cells in Cat Primary Visual Cortex. *The Journal of Neuroscience* **21,** 4002–4015.

Anastassiou CA, Perin R, Buzsáki G, Markram H & Koch C (2015). Cell type- and activity-dependent extracellular correlates of intracellular spiking. *Journal of Neurophysiology* **114,** 608–623.

Azouz R, Gray CM, Nowak LG & McCormick DA (1997). Physiological properties of inhibitory interneurons in cat striate cortex. *Cerebral cortex (New York, NY: 1991)* **7,** 534–545.

Bakkum DJ, Frey U, Radivojevic M, Russell TL, Müller J, Fiscella M, Takahashi H & Hierlemann A (2013). Tracking axonal action potential propagation on a high-density microelectrode array across hundreds of sites. *Nature Communications*; DOI: 10.1038/ncomms3181.

Baranyi A, Szente MB & Woody CD (1993). Electrophysiological characterization of different types of neurons recorded in vivo in the motor cortex of the cat. II. Membrane parameters, action potentials, current-induced voltage responses and electrotonic structures. *Journal of Neurophysiology* **69,** 1865–1879.

Barry JM (2015). Axonal activity in vivo: technical considerations and implications for the exploration of neural circuits in freely moving animals. *Frontiers in Neuroscience*; DOI: 10.3389/fnins.2015.00153.

Barthó P, Hirase H, Monconduit L, Zugaro M, Harris KD & Buzsáki G (2004). Characterization of Neocortical Principal Cells and Interneurons by Network Interactions and Extracellular Features. *Journal of Neurophysiology* **92,** 600–608.

Blanche TJ, Spacek MA, Hetke JF & Swindale NV (2005). Polytrodes: High-Density Silicon Electrode Arrays for Large-Scale Multiunit Recording. *Journal of Neurophysiology* **93,** 2987–3000.

Bullier J (2001). Integrated model of visual processing. *Brain Research Reviews* **36,** 96–107.

Bullier J & Henry GH (1979). Ordinal position of neurons in cat striate cortex. *Journal of Neurophysiology* **42,** 1251–1263.

Bullier J, Mustari MJ & Henry GH (1982). Receptive-field transformations between LGN neurons and S-cells of cat-striate cortex. *Journal of Neurophysiology* **47,** 417–438.

Buzsáki G (2004). Large-scale recording of neuronal ensembles. *Nat Neurosci* **7,** 446–451.

Cai D, DeAngelis GC & Freeman RD (1997). Spatiotemporal receptive field organization in the lateral geniculate nucleus of cats and kittens. *Journal of neurophysiology* **78,** 1045–1061.

This article is protected by copyright. All rights reserved.

Author Manuscript

Cappe C, Rouiller EM & Barone P (2009). Multisensory anatomical pathways. *Hearing Research* **258,** 28–36.

Chapman B, Zahs KR & Stryker MP (1991). Relation of cortical cell orientation selectivity to alignment of receptive fields of the geniculocortical afferents that arborize within a single orientation column in ferret visual cortex. *J Neurosci* **11,** 1347–1358.

Chen K, Ding A-M, Liang X-H, Zhang L-P, Wang L & Song X-M (2015). Effect of Contrast on Visual Spatial Summation in Different Cell Categories in Cat Primary Visual Cortex ed. Nishijo H. *PLOS ONE* **10,** e0144403.

Constantinople CM, Disney AA, Maffie J, Rudy B & Hawken MJ (2009). Quantitative analysis of neurons with Kv3 potassium channel subunits, Kv3.1b and Kv3.2, in macaque primary visual cortex. *Journal of Comparative Neurology* **516,** 291–311.

Feldman R & Sanger J (2007). *The Text Mining Handbook: Advanced Approaches in Analyzing Unstructured Data*. Cambridge University Press.

Gentet LJ, Avermann M, Matyas F, Staiger JF & Petersen CCH (2010). Membrane Potential Dynamics of GABAergic Neurons in the Barrel Cortex of Behaving Mice. *Neuron* **65,** 422–435.

Gharat A & Baker CL (2017). Nonlinear Y-Like Receptive Fields in the Early Visual Cortex: An Intermediate Stage for Building Cue-Invariant Receptive Fields from Subcortical Y Cells. *The Journal of Neuroscience* **37,** 998–1013.

Gold C, Girardin CC, Martin KAC & Koch C (2009). High-Amplitude Positive Spikes Recorded Extracellularly in Cat Visual Cortex. *Journal of Neurophysiology* **102,** 3340–3351.

Gold C, Henze DA, Koch C & Buzsáki G (2006). On the Origin of the Extracellular Action Potential Waveform: A Modeling Study. *Journal of Neurophysiology* **95,** 3113–3128.

Gonzalez RC & Woods RE (2008). Digital image processing (International ed.). *ed: Upper Saddle River, NJ: Prentice Hall*.

Grundy D (2015). Principles and standards for reporting animal experiments in The Journal of Physiology and Experimental Physiology. *Experimental Physiology* **100,** 755–758.

Guido W & Weyand T (1995). Burst responses in thalamic relay cells of the awake behaving cat. *Journal of Neurophysiology* **74,** 1782–1786.

Gur M, Beylin A & Snodderly DM (1999). Physiological Properties of Macaque V1 Neurons are Correlated With Extracellular Spike Amplitude, Duration, and Polarity. *Journal of Neurophysiology* **82,** 1451–1464.

Hartigan JA & Hartigan PM (1985). The Dip Test of Unimodality. *The Annals of Statistics* **13,** 70–84.

Hastie T, Tibshirani R & Friedman J (2009). *The Elements of Statistical Learning: Data Mining, Inference, and Prediction, Second Edition*, 2nd edn. Springer-Verlag, New York. Available at: https://www.springer.com/gp/book/9780387848570 [Accessed November 18, 2019].

Heinricher MM (2004). Principles of extracellular single-unit recording. *Microelectrode Recording in Movement Disorder Surgery*.

This article is protected by copyright. All rights reserved.

Henry GH, Harvey AR & Lund JS (1979). The afferent connections and laminar distribution of cells in the cat striate cortex. *Journal of Comparative Neurology* **187,** 725–744.

Henze DA, Borhegyi Z, Csicsvari J, Mamiya A, Harris KD & Buzsáki G (2000). Intracellular Features Predicted by Extracellular Recordings in the Hippocampus In Vivo. *Journal of Neurophysiology* **84,** 390–400.

Hochstein S & Shapley RM (1976). Linear and nonlinear spatial subunits in Y cat retinal ganglion cells. *The Journal of Physiology* **262,** 265–284.

Hubel DH & Livingstone MS (1981). Regions of poor orientation tuning coincide with patches of cytochrome oxidase staining in monkey striate cortex. In *Neuroscience Abstracts.*

Hubel DH & Wiesel TN (1959). Receptive fields of single neurones in the cat's striate cortex. *The Journal of physiology* **148,** 574–591.

Hubel DH & Wiesel TN (1961). Integrative action in the cat's lateral geniculate body. *The Journal of Physiology* **155,** 385–398.

Hubel DH & Wiesel TN (1962). Receptive fields, binocular interaction and functional architecture in the cat's visual cortex. *The Journal of physiology* **160,** 106–154.

Ichinohe N, Watakabe A, Miyashita T, Yamamori T, Hashikawa T & Rockland KS (2004). A voltage-gated potassium channel, Kv3. 1b, is expressed by a subpopulation of large pyramidal neurons in layer 5 of the macaque monkey cortex. *Neuroscience* **129,** 179–185.

Jenkinson SG (1993). Oxygen toxicity. *New horizons (Baltimore, Md)* **1,** 504–511.

Jia XX, Siegle JH, Bennett C, Gale SD, Denman DJ, Koch C & Olsen SR (2019). High-density extracellular probes reveal dendritic backpropagation and facilitate neuron classification. *J Neurophysiol*17.

Jin JZ, Weng C, Yeh C-I, Gordon JA, Ruthazer ES, Stryker MP, Swadlow HA & Alonso J-M (2008). On and off domains of geniculate afferents in cat primary visual cortex. *Nature Neuroscience* **11,** 88–94.

Kara P, Pezaris JS, Yurgenson S & Reid RC (2002). The spatial receptive field of thalamic inputs to single cortical simple cells revealed by the interaction of visual and electrical stimulation. *PNAS* **99,** 16261–16266.

Kelly RC, Smith MA, Samonds JM, Kohn A, Bonds AB, Movshon JA & Sing Lee T (2007). Comparison of Recordings from Microelectrode Arrays and Single Electrodes in the Visual Cortex. *Journal of Neuroscience* **27,** 261–264.

Leventhal AG, Wang Y, Pu M, Zhou Y & Ma Y (2003). GABA and Its Agonists Improved Visual Cortical Function in Senescent Monkeys. *Science* **300,** 812–815.

Lewandowska MK, Bakkum DJ, Rompani SB & Hierlemann A (2015). Recording Large Extracellular Spikes in Microchannels along Many Axonal Sites from Individual Neurons ed. Martinoia S. *PLOS ONE* **10,** e0118514.

Lloyd S (1982). Least squares quantization in PCM. *IEEE Transactions on Information Theory* **28,** 129–137.

This article is protected by copyright. All rights reserved.

Author Manuscript

Lund JS, Henry GH, Macqueen CL & Harvey AR (1979). Anatomical organization of the primary visual cortex (area 17) of the cat. A comparison with area 17 of the macaque monkey. *The Journal of Comparative Neurology* **184,** 599–618.

Maaten L van der & Hinton G (2008). Visualizing data using t-SNE. *Journal of machine learning research* **9,** 2579–2605.

Mallat SG (1989). A theory for multiresolution signal decomposition: the wavelet representation. *IEEE Transactions on Pattern Analysis and Machine Intelligence* **11,** 674–693.

Martina M & Jonas P (1997). Functional differences in Na+ channel gating between fast-spiking interneurones and principal neurones of rat hippocampus. *J Physiol* **505,** 593–603.

Martina M, Schultz JH, Ehmke H, Monyer H & Jonas P (1998). Functional and Molecular Differences between Voltage-Gated K+ Channels of Fast-Spiking Interneurons and Pyramidal Neurons of Rat Hippocampus. *J Neurosci* **18,** 8111–8125.

Martinez LM, Wang Q, Reid RC, Pillai C, Alonso J-M, Sommer FT & Hirsch JA (2005). Receptive field structure varies with layer in the primary visual cortex. *Nature Neuroscience* **8,** 372–379.

McFarland JM, Cui Y & Butts DA (2013). Inferring Nonlinear Neuronal Computation Based on Physiologically Plausible Inputs ed. Bethge M. *PLoS Computational Biology* **9,** e1003143.

Niell CM & Stryker MP (2008). Highly Selective Receptive Fields in Mouse Visual Cortex. *Journal of Neuroscience* **28,** 7520–7536.

Nowak LG, Sanchez-Vives MV & McCormick DA (2008). Lack of Orientation and Direction Selectivity in a Subgroup of Fast-Spiking Inhibitory Interneurons: Cellular and Synaptic Mechanisms and Comparison with Other Electrophysiological Cell Types. *Cereb Cortex* **18,** 1058–1078.

Onorato I, Neuenschwander S, Hoy J, Lima B, Rocha K-S, Broggini AC, Uran C, Spyropoulos G, Womelsdorf T & Fries P (2019). A distinct class of bursting neurons with strong gamma synchronization and stimulus selectivity in monkey V1. *bioRxiv*583955.

Ouellette BG & Casanova C (2006). Overlapping visual response latency distributions in visual cortices and LP-pulvinar complex of the cat. *Exp Brain Res* **175,** 332–341.

Pachitariu M, Steinmetz N, Kadir S, Carandini M & Harris KD (2016). Kilosort: realtime spike-sorting for extracellular electrophysiology with hundreds of channels. ; DOI: 10.1101/061481.

Pan L, Alagapan S, Franca E, DeMarse T, Brewer GJ & Wheeler BC (2014). Large Extracellular Spikes Recordable From Axons in Microtunnels. *IEEE Transactions on Neural Systems and Rehabilitation Engineering* **22,** 453–459.

Petrusca D, Grivich MI, Sher A, Field GD, Gauthier JL, Greschner M, Shlens J, Chichilnisky EJ & Litke AM (2007). Identification and Characterization of a Y-Like Primate Retinal Ganglion Cell Type. *Journal of Neuroscience* **27,** 11019–11027.

Pettigrew JD, Nikara T & Bishop PO (1968). Binocular interaction on single units in cat striate cortex: Simultaneous stimulation by single moving slit with receptive fields in correspondence. *Exp Brain Res* **6,** 391–410.

Price NS (n.d.). NicPrice.net. Available at: http://www.nicprice.net/diptest/ [Accessed May 4, 2020].

This article is protected by copyright. All rights reserved.

Author Manuscript

Raastad M & Shepherd GMG (2003). Single-axon action potentials in the rat hippocampal cortex. *The Journal of Physiology* **548,** 745–752.

Reid RC & Alonso J-M (1995). Specificity of monosynaptic connections from thalamus to visual cortex. *Nature* **378,** 281–284.

Ringach DL (2002). Spatial Structure and Symmetry of Simple-Cell Receptive Fields in Macaque Primary Visual Cortex. *Journal of Neurophysiology* **88,** 455–463.

Ringach DL, Hawken MJ & Shapley R (2003). Dynamics of Orientation Tuning in Macaque V1: The Role of Global and Tuned Suppression. *Journal of Neurophysiology* **90,** 342–352.

Ringach DL, Shapley RM & Hawken MJ (2002). Orientation Selectivity in Macaque V1: Diversity and Laminar Dependence. *The Journal of Neuroscience* **22,** 5639–5651.

Robbins AA, Fox SE, Holmes GL, Scott RC & Barry JM (2013). Short duration waveforms recorded extracellularly from freely moving rats are representative of axonal activity. *Front Neural Circuits*; DOI: 10.3389/fncir.2013.00181.

Rosenberg A, Husson TR & Issa NP (2010). Subcortical Representation of Non-Fourier Image Features. *J Neurosci* **30,** 1985–1993.

Rossant C, Kadir SN, Goodman DFM, Schulman J, Hunter MLD, Saleem AB, Grosmark A, Belluscio M, Denfield GH, Ecker AS, Tolias AS, Solomon S, Buzsáki G, Carandini M & Harris KD (2016). Spike sorting for large, dense electrode arrays. *Nat Neurosci* **19,** 634–641.

Rust NC, Schwartz O, Movshon JA & Simoncelli E (2004). Spike-triggered characterization of excitatory and suppressive stimulus dimensions in monkey V1. *Neurocomputing* **58–60,** 793–799.

Schmolesky MT, Wang Y, Hanes DP, Thompson KG, Leutgeb S, Schall JD & Leventhal AG (1998). Signal Timing Across the Macaque Visual System. *Journal of Neurophysiology* **79,** 3272–3278.

Schwartz O, Pillow JW, Rust NC & Simoncelli EP (2006). Spike-triggered neural characterization. *Journal of Vision* **6,** 13.

Skottun BC, De Valois RL, Grosof DH, Movshon JA, Albrecht DG & Bonds AB (1991). Classifying simple and complex cells on the basis of response modulation. *Vision Research* **31,** 1078–1086.

Snider RK, Kabara JF, Roig BR & Bonds AB (1998). Burst Firing and Modulation of Functional Connectivity in Cat Striate Cortex. *Journal of Neurophysiology* **80,** 730–744.

Steffey EP, Gillespie JR, Berry JD & Eger EI (1974). Anesthetic potency (MAC) of nitrous oxide in the dog, cat, and stump-tail monkey. 3.

Stringer C, Pachitariu M, Steinmetz N, Reddy CB, Carandini M & Harris KD (2019). Spontaneous behaviors drive multidimensional, brainwide activity. *Science*; DOI: 10.1126/science.aav7893.

Suematsu N, Naito T & Sato H (2012). Relationship between orientation sensitivity and spatiotemporal receptive field structures of neurons in the cat lateral geniculate nucleus. *Neural Networks* **35,** 10–20.

This article is protected by copyright. All rights reserved.

Author Manuscript

Talebi V & Baker CL (2016). Categorically distinct types of receptive fields in early visual cortex. *Journal of Neurophysiology* **115,** 2556–2576.

Touryan J, Felsen G & Dan Y (2005). Spatial structure of complex cell receptive fields measured with natural images. *Neuron* **45,** 781–791.

Van Hooser SD (2007). Similarity and Diversity in Visual Cortex: Is There a Unifying Theory of Cortical Computation? *Neuroscientist* **13,** 639–656.

Vidyasagar TR, Jayakumar J, Lloyd E & Levichkina EV (2015). Subcortical orientation biases explain orientation selectivity of visual cortical cells. *Physiological Reports* **3,** e12374.

Vigneswaran G, Kraskov A & Lemon RN (2011). Large Identified Pyramidal Cells in Macaque Motor and Premotor Cortex Exhibit "Thin Spikes": Implications for Cell Type Classification. *Journal of Neuroscience* **31,** 14235–14242.

Villeneuve MY & Casanova C (2003). On the use of isoflurane versus halothane in the study of visual response properties of single cells in the primary visual cortex. *Journal of Neuroscience Methods* **129,** 19–31.

Vries SEJ de et al. (2020). A large-scale standardized physiological survey reveals functional organization of the mouse visual cortex. *Nat Neurosci* **23,** 138–151.

Wang W, Jones HE, Andolina IM, Salt TE & Sillito AM (2006). Functional alignment of feedback effects from visual cortex to thalamus. *Nature neuroscience* **9,** 1330.

Yosinski J, Clune J, Nguyen A, Fuchs T & Lipson H (2015). Understanding Neural Networks Through Deep Visualization. *arXiv:150606579 [cs]*. Available at: http://arxiv.org/abs/1506.06579 [Accessed February 6, 2020].

Author Manuscript

This article is protected by copyright. All rights reserved.